nature cardiovascular research

Article

https://doi.org/10.1038/s44161-022-00199-2

Live-cell photoactivated localization microscopy correlates nanoscale ryanodine receptor configuration to calcium sparks in cardiomyocytes

Received: 7 July 2021

Accepted: 24 November 2022

Published online: 15 March 2023

Check for updates

Yufeng Hou[1,5] ✉, Martin Laasmaa[1,5], Jia Li[1], Xin Shen[1], Ornella Manfra[1], Einar S. Nordén[1,2], Christopher Le[1], Lili Zhang[1,2], Ivar Sjaastad[1,2], Peter P. Jones[3], Christian Soeller[4] & William E. Louch[1,2] ✉

Ca^{2+} sparks constitute the fundamental units of Ca^{2+} release in cardiomyocytes. Here we investigate how ryanodine receptors (RyRs) collectively generate these events by employing a transgenic mouse with a photoactivated label on RyR2. This allowed correlative imaging of RyR localization, by super-resolution photoactivated localization microscopy, and Ca^{2+} sparks, by high-speed imaging. Two populations of Ca^{2+} sparks were observed: stationary events and 'traveling' events that spread between neighboring RyR clusters. Traveling sparks exhibited up to eight distinct releases, sourced from local or distal junctional sarcoplasmic reticulum. Quantitative analyses showed that sparks may be triggered by any number of RyRs within a cluster, and that acute β-adrenergic stimulation augments intracluster RyR recruitment to generate larger events. In contrast, RyR 'dispersion' during heart failure facilitates the generation of traveling sparks. Thus, RyRs cooperatively generate Ca^{2+} sparks in a complex, malleable fashion, and channel organization regulates the propensity for local propagation of Ca^{2+} release.

Regulation of intracellular Ca^{2+} is essential to excitation–contraction coupling in cardiomyocytes. During the action potential, Ca^{2+} influx via L-type Ca^{2+} channels in the surface membrane and t-tubules triggers the opening of apposed RyRs in the sarcoplasmic reticulum (SR). Resulting Ca^{2+} release from RyRs occurs in fundamental units called Ca^{2+} sparks[1]. The spatiotemporal summation of these events across the cell produces the Ca^{2+} transient which, in turn, triggers cellular contraction.

While the basic process of Ca^{2+}-induced Ca^{2+} release in cardiomyocytes is well established, the precise manner by which RyRs cooperatively generate Ca^{2+} sparks has remained unclear. However, an emerging view is that RyR recruitment is intimately linked to the nanoscale arrangement of the channels[2–4]. As RyRs are large and electron-dense, early electron microscopy studies successfully identified their presence within narrow dyadic junctions between the sarcolemmal and SR membranes[5,6]. These studies suggested that RyRs were tightly packed in crystalline arrays; a view which has been disputed by more recent work using electron microscopy tomography[7,8], super-resolution imaging[9,10] and expansion microscopy[11]. Indeed, current thinking is that dyads are not completely filled with RyRs, but that the channels are rather localized within multiple RyR clusters[7–9]. Within these clusters,

[1]Institute for Experimental Medical Research, Oslo University Hospital and University of Oslo, Oslo, Norway. [2]K.G. Jebsen Centre for Cardiac Research, University of Oslo, Oslo, Norway. [3]Department of Physiology, School of Biomedical Sciences and HeartOtago, University of Otago, Dunedin, New Zealand. [4]Department of Physiology, University of Bern, Bern, Switzerland. [5]These authors contributed equally: Yufeng Hou, Martin Laasmaa. ✉e-mail: yhou021@gmail.com; w.e.louch@medisin.uio.no

https://doi.org/10.1038/s44161-022-00199-2

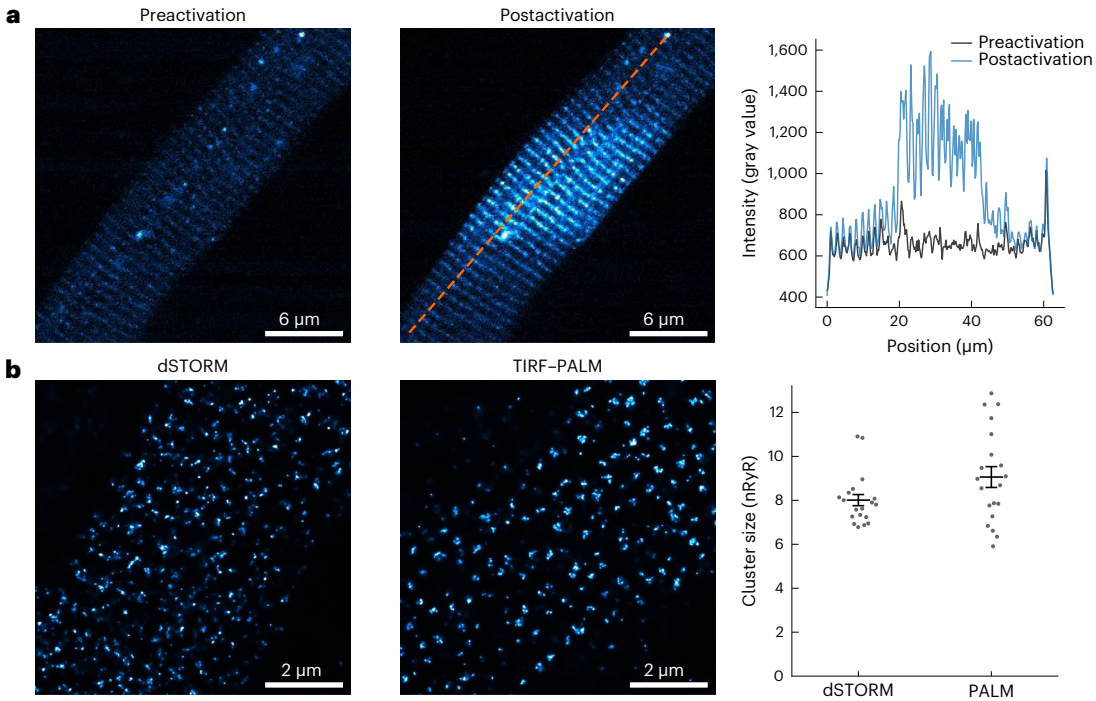

Fig. 1 | Demonstration of live-cell PALM imaging in RFP RyR cardiomyocytes. a, Effects of photoactivation. Minimal fluorescence was observed at 543 nm at baseline (left). Photoactivation was achieved using brief (30 s) low-intensity illumination with a 405 nm confocal laser, resulting in a robust fluorescence signal increase within the illuminated band across the center of the cell. An intensity plot measured along the dotted orange line illustrates regional RyR photoactivation (right). **b**, Super-resolution RyR images obtained by fixed-cell surface dSTORM (left) and live-cell TIRF–PALM (middle). dSTORM and PALM measurements showed similar RyR organization on the cell surface, as indicated by measurements of cluster sizes (right). Data are presented as mean ± s.e.m. Difference between groups was tested with two-tailed linear mixed models nested by cell and animal levels. n_{dSTORM} = 3 animals, 20 cells; n_{PALM} = 3 animals, 20 cells.

neighboring channels are in molecular proximity, and the clusters themselves exhibit complex arrangements in three-dimensional space. It has been proposed that neighboring clusters of RyRs may collectively generate Ca^{2+} sparks, if the diffusion distances between them are sufficiently short[2,12,13]. Thus, multiple RyR clusters could be envisioned to constitute a 'Ca^{2+} release unit' or 'supercluster'; two terms that are used synonymously below. This concept has important implications for understanding plasticity of excitation–contraction coupling, as recent data have indicated that RyR arrangements are dynamic[8,14–16], and altered during pathological states such as atrial fibrillation[17] and heart failure (HF)[2,11,16].

Experimental investigation of RyR cooperativity during Ca^{2+} spark formation has thus far been obstructed by technical limitations. High-resolution imaging techniques capable of resolving RyRs, such as direct stochastic optical reconstruction microscopy (dSTORM), DNA points accumulation for imaging in nanoscale topography (DNA-PAINT) and electron microscopy, typically require fixed samples. Furthermore, live-cell analysis of Ca^{2+} dynamics in two-dimensional (2D) space requires high-speed imaging, while most traditional confocal microscopes can only obtain such temporal resolution with one-dimensional (1D) line-scan imaging. In the present work, we circumvented these technical hurdles by employing a knock-in mouse expressing photoactivated red fluorescent protein (PA-RFP) affixed to RyR2, allowing us to perform live-cell super-resolution photoactivated localization microscopy (PALM) of RyR positions. Correlative high-speed Ca^{2+} imaging linked RyR locations to the temporal and spatial characteristics of Ca^{2+} sparks. These analyses revealed that Ca^{2+} release events frequently propagate between multiple RyR clusters, resulting in 'traveling' sparks. We further observed that β-adrenergic stimulation increases intracluster RyR recruitment to produce larger events, while RyR cluster 'dispersion' during HF promotes the occurrence of traveling sparks.

Results

Creation of transgenic PA-RFP RyR mouse line

A transgenic mouse was created with PA-RFP affixed to the 'clamp' region of RyR2 at T1365 (Extended Data Fig. 1). Previous work has shown that fluorescent proteins tagged to this location do not disrupt in vivo or cardiomyocyte function[18]. We presently confirmed that both animal and heart weights were normal in PA-RFP RyR mice (Extended Data Fig. 2a). In cardiomyocytes isolated from PA-RFP hearts, we observed Ca^{2+} transients that were remarkably similar to those from wild-type mice (Extended Data Fig. 2b,c).

Demonstration of live-cell PALM imaging of RyRs

We next sought to establish the suitability of PA-RFP cardiomyocytes for live-cell analysis of RyR localization. Confocal imaging of these cells revealed minimal fluorescence in the 561 nm channel before photoactivation (Fig. 1a, left panel). However, directed photoactivation with a 405 nm laser resulted in a prominent increase in 561 nm fluorescence along Z-lines where RyR localization is anticipated (middle and right panels). To quantitatively assess the arrangement of RyRs, we employed super-resolution, total internal reflection fluorescence (TIRF) imaging at the cell surface, where a relatively flat arrangement of the channels simplifies their counting[9,19]. Photoswitching experiments for PALM imaging in live PA-RFP cardiomyocytes revealed a rather punctate and scattered RyR arrangement (Fig. 1b). A similar RyR organization was observed in dSTORM images of fixed cardiomyocytes, where RyRs were labeled by immunohistochemistry. Indeed, a quantitative comparison of RyR cluster sizes measured by the two

techniques revealed similar mean cluster sizes (Fig. 1b, right panel). Thus, live-cell super-resolution of RyR localization is feasible and enables RyR localization analysis that is comparable with dSTORM imaging of fixed cells (~45 nm versus ~20 nm resolution based on Fourier ring correlation, Extended Data Fig. 3).

Single-release and multiple-release Ca^{2+} sparks

As we aimed to link RyR localization and function in live cardiomyocytes, we next developed techniques to enable rapid, 2D imaging and detection of Ca^{2+} sparks at the cell surface. Cardiomyocytes were loaded with the Ca^{2+}-sensitive dye Cal520-AM, and imaged by TIRF at 2 ms per frame. To identify sparks from raw data, we developed a custom detection algorithm (see Methods, Extended Data Fig. 4 and Supplementary Table 1). We restricted our analyses to in-focus Ca^{2+} release events using full width half maximum measurements, as our mathematical modeling supported that events wider than ~0.8 µm likely result from out-of-plane release sites (Extended Data Fig. 5).

Representative time-series recordings of detected sparks are presented in Fig. 2a,b (upper panels), with the spark centroid indicated by a red dot in each frame, and localization uncertainty indicated by the surrounding white circle. As Ca^{2+} release occurs far more quickly than its reuptake and removal from the cell, the actual site for Ca^{2+} released in a given frame is partially masked by the lingering, previously released Ca^{2+}. Therefore, to better identify the true site and timing of Ca^{2+} release, we implemented the 'CaCLEAN' diffusion-subtraction (DS) method developed by the Lipp group[20]. With this approach, Ca^{2+} images are first convolved with a Gaussian function to estimate the expected diffusion distance between each frame and its subsequent frame. This convolved image is then subtracted from the subsequent frame to produce a DS image, estimating only the newly released Ca^{2+} signal. Examples of this processing are presented below the raw $\Delta F/F_0$ recordings in Fig. 2a,b. DS enabled identification of short Ca^{2+} release pulses, which are plotted within the time course of the overall Ca^{2+} spark (lower panels).

When we applied our detection algorithm and DS method, we identified two distinct types of spark events: single and multirelease sparks. Single-release sparks comprised a solitary, continuous release event (Fig. 2a), while multirelease sparks exhibited several, temporally separated releases (Fig. 2b). Of all the Ca^{2+} sparks, 15.0% exhibited multiple releases, and these comprised between two and eight distinct events. The average number of release events per spark was 1.59 ± 0.07 for all recordings. Importantly, while single-release sparks remained relatively stationary, multirelease events were frequently observed to 'travel' during the spark time course. This is illustrated in the example shown in Fig. 2b, as a marked leftward displacement of 300 nm occurred as Ca^{2+} release was consecutively triggered at two discrete locations. We calculated this movement using the fitted centroid positions to determine the 'radius of gyration', often used in analysis of human mobility in geographical studies[21], to describe how far Ca^{2+} release centroids are removed from the spark center of mass (Fig. 2c). Importantly, the magnitude of DS release events was similar in single- and multirelease sparks (Fig. 2c). Nevertheless, the spatiotemporal summation of individual releases during multirelease sparks resulted in larger magnitude and longer-lasting Ca^{2+} release than in single-release sparks (Fig. 2c).

As we recorded Ca^{2+} sparks in two spatial dimensions rather than by more conventional 1D confocal line-scan imaging, we examined how measured multirelease sparks would have appeared in line-scan mode. We observed that line-scans rendered from recorded multirelease sparks produced very different spark profiles depending on the position of the scan line. This is illustrated in Fig. 2d, with the scan line placed along several vertical (V) or horizontal (H) positions. Depending on line position, some spark profiles captured only one of the release events, resulting in a 'normal' spark profile (Fig. 2d, example V2). Other positions captured both events, and revealed profiles that would likely have been classified as 'macro sparks' or 'slow sparks' in previous line-scan studies (Fig. 2d, examples H1, H2, respectively). In this example, classification as a macro spark is incorrect as the two sites of Ca^{2+} release are closer together than release points that generate macro sparks (that is, RyRs ≈1.8 µm apart at neighboring Z-lines). Also, characterization of the release as a 'slow spark' implies protracted release without appreciation that it includes summation of distinct release events at different sites. Thus, 'traveling' multirelease sparks have likely been overlooked or misidentified in previous work.

Correlation of Ca^{2+} sparks to local RyR clusters

We next combined Ca^{2+} spark and RyR imaging to link RyR organization and function. Ca^{2+} spark recording was performed first, followed by PALM super-resolution imaging of RyRs within the same area of the cell to map each spark to its origin. For this approach, RyR clusters were defined as individual areas where there was a contiguous, thresholded PALM signal. A representative example of such correlation is presented in Fig. 3a for a single-release Ca^{2+} spark. This example shows that the centroid of the released Ca^{2+} clearly superimposed on an RyR cluster. Overall, we noted that ~80% of all release events were situated within 300 nm of a cluster (dashed line in Fig. 3c). This value is equivalent to the theoretical resolution of imaging Cal520 fluorescence >570 nm (238 nm) plus the predicted fitting error for localizing the spark centroid (65 nm, Extended Data Fig. 6). Thus, our method enables robust pairing of RyR organization and function.

Performing similar correlation analysis for multirelease sparks, we observed that the more complex Ca^{2+} release pattern during these events interfered with their mapping to RyR clusters. For example, in the recording shown in Fig. 3b, the centroid of the raw fluorescence data was detected between several clusters. However, DS applied to the raw data (Fig. 3b, bottom right row) effectively removed interference from latent Ca^{2+}, revealing that Ca^{2+} release in fact moved between two neighboring clusters. This observation supports that Ca^{2+} sparks routinely involve the cooperative opening of neighboring RyR clusters.

We further verified the mobile nature of Ca^{2+} sparks by visualizing the junctional SR (jSR), using background Cal520 fluorescence. Figure 3d

Fig. 2 | Single- and multiple-release Ca^{2+} sparks. TIRF imaging of cells loaded with Cal520-AM revealed two types of Ca^{2+} sparks. **a**, Single-release Ca^{2+} spark. Representative raw recordings of a spark time course are presented above DS images. The centroid of the Ca^{2+} signal for each frame is indicated by a red dot, with the surrounding white circle estimating localization uncertainty within the 300-nm diffraction limit. Contours indicate fitting dimensions corresponding to five levels between the 70th signal percentile and peak spark amplitude. The overall spark time course is indicated in the lower panel, with new Ca^{2+} released since the previous frame indicated as an orange bar, and the duration of spark detection shown in gray. 0 ms on the time axis is set as the point of earliest spark detection (>2 s.d. above background). **b**, Multiple-release Ca^{2+} spark. In a subset of recorded sparks, multiple releases were observed, separated by at least one frame where no Ca^{2+} release occurred. **c**, Comparison of properties of single- and multirelease sparks. From left to right: radius of gyration (as a measure of centroid movement), amplitude, TTP, FDHM and DS $\Delta F/F_0$. Data are presented as mean ± s.e.m. Differences between groups were tested with two-tailed linear mixed models with Tukey post hoc correction for multiple comparisons. Significance levels: $^{*}P < 0.05$, $^{**}P < 0.01$, $^{***}P < 0.001$. *P* values: radius of gyration = 1.11×10^{-5}, DS amplitude = 0.0601, amplitude = 0.0395, TTP < 2×10^{-16}, FDHM = 7.5×10^{-15}. For *n* values, see Source data. **d**, Simulation of 1D line-scans reveals mischaracterization of multirelease sparks. Slices were made along various axes in the vertical (V) or horizontal (H) orientation across a region with multiple releases (2D image shows pixel-wise maximal intensity during the spark). Corresponding line-scans and measured spark time courses are illustrated.

https://doi.org/10.1038/s44161-022-00199-2

shows jSR in red, with superimposed RyR clusters (blue) and spark centroids (crosses). We qualitatively observed that multirelease sparks showing small movements (<300 nm) tended to remain within the same jSR (Fig. 3d, middle panel), whereas those with larger movements (that is 'traveling sparks') frequently jumped to a neighboring jSR (right panel).

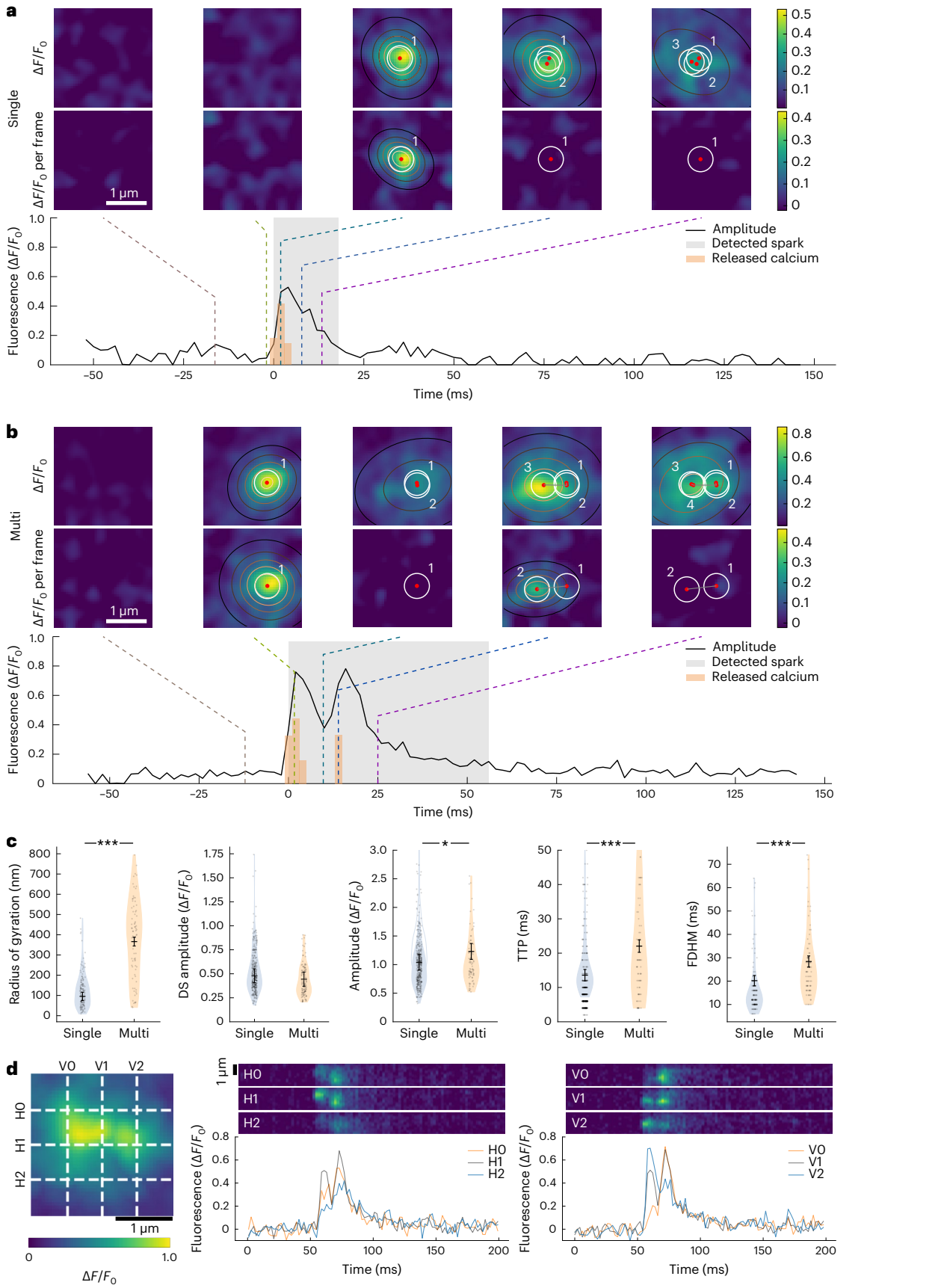

https://doi.org/10.1038/s44161-022-00199-2

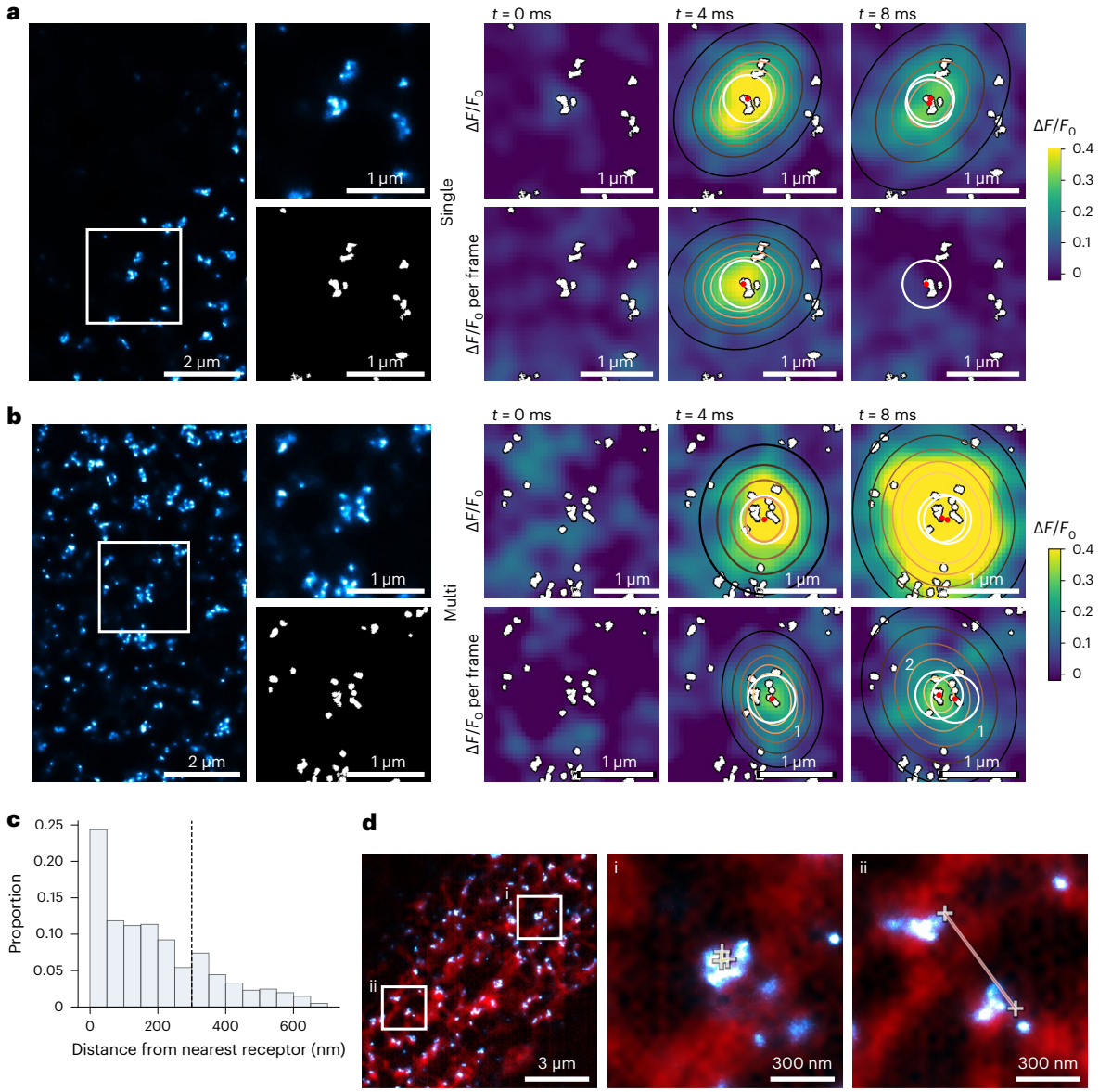

Fig. 3 | Correlation of single- and multiple-release Ca^{2+} sparks to RyR clusters. a, Super-resolution PALM imaging of RyRs at the cell surface (left) with enlargement of the indicated region and adaptive thresholding. Correlative Ca^{2+} imaging revealed superimposition of a Ca^{2+} spark centroid (red dot, localization uncertainty is indicated by a white circle) to an RyR cluster (right, upper panels). DS analyses revealed only a single Ca^{2+} release pulse at 4 ms, and no further release at 8 ms (lower right panels). **b**, For multiple-release Ca^{2+} sparks, DS improved mapping to RyR cluster origins, and revealed 'traveling' of Ca^{2+} release between adjacent clusters. In the presented example, distinct release events occurred at 4 ms and 8 ms, which summated to generate a large Ca^{2+} spark. **c**, Histogram showing distance from the centroid of each DS release event to the nearest RyR cluster. Dotted line indicates the expected localization accuracy of 300 nm, used as a cutoff for subsequent correlation analysis. $n = 4$ animals, 11 cells, 359 sparks, 608 frames. **d**, Left, visualization of the jSR using background Cal520 fluorescence (red), together with RyR positions (white) and Ca^{2+} release events (white crosses). Multiple-release sparks were observed to remain within the same jSR (middle) or travel to distant jSR (right). Experiments in **a**, **b** and **d** were repeated independently in cells from four hearts with similar results.

Quantitative analysis of Ca^{2+} release sites

RyR counting performed on thresholded PALM images enabled further relation of Ca^{2+} spark characteristics to their RyR cluster(s) of origin. As the size of individual RyRs is close to the attained resolution of the PALM imaging, the number of RyRs within each cluster needed to be estimated. We took two approaches to this task; the first of which predicted the number of RyRs within clusters based on tight, grid-like packing of RyRs within the thresholded area (Fig. 4a), as has been done in previous dSTORM studies[9,22]. We also estimated RyR numbers assuming looser packing, utilizing RyR density measurements reported in a recent DNA-PAINT study[10] (Extended Data Fig. 7). Using either approach, when we examined the sizes of clusters that produce Ca^{2+} sparks, we found that single-release sparks (blue) originate from fairly small RyR clusters, similar to the general cluster size distribution (red, Fig. 4a and Extended Data Fig. 7a). Multirelease sparks, however, tended to be linked to larger RyR clusters (orange). Indeed, assuming tight RyR packing, mean nearest cluster size was 19 ± 2 RyRs for multirelease sparks versus 13 ± 2 RyRs for single-release events (Fig. 4b, left panel, see Extended Data Fig. 7b for equivalent values assuming loose RyR packing).

We additionally examined the local RyR density at each spark's origin, within an area defined by the fitted spark Gaussian (centroid position ±2 s.d.). We weighted these measurements based on RyR proximity, to give preferential contribution to RyRs nearer the spark center (Methods). These analyses showed that, in comparison

https://doi.org/10.1038/s44161-022-00199-2

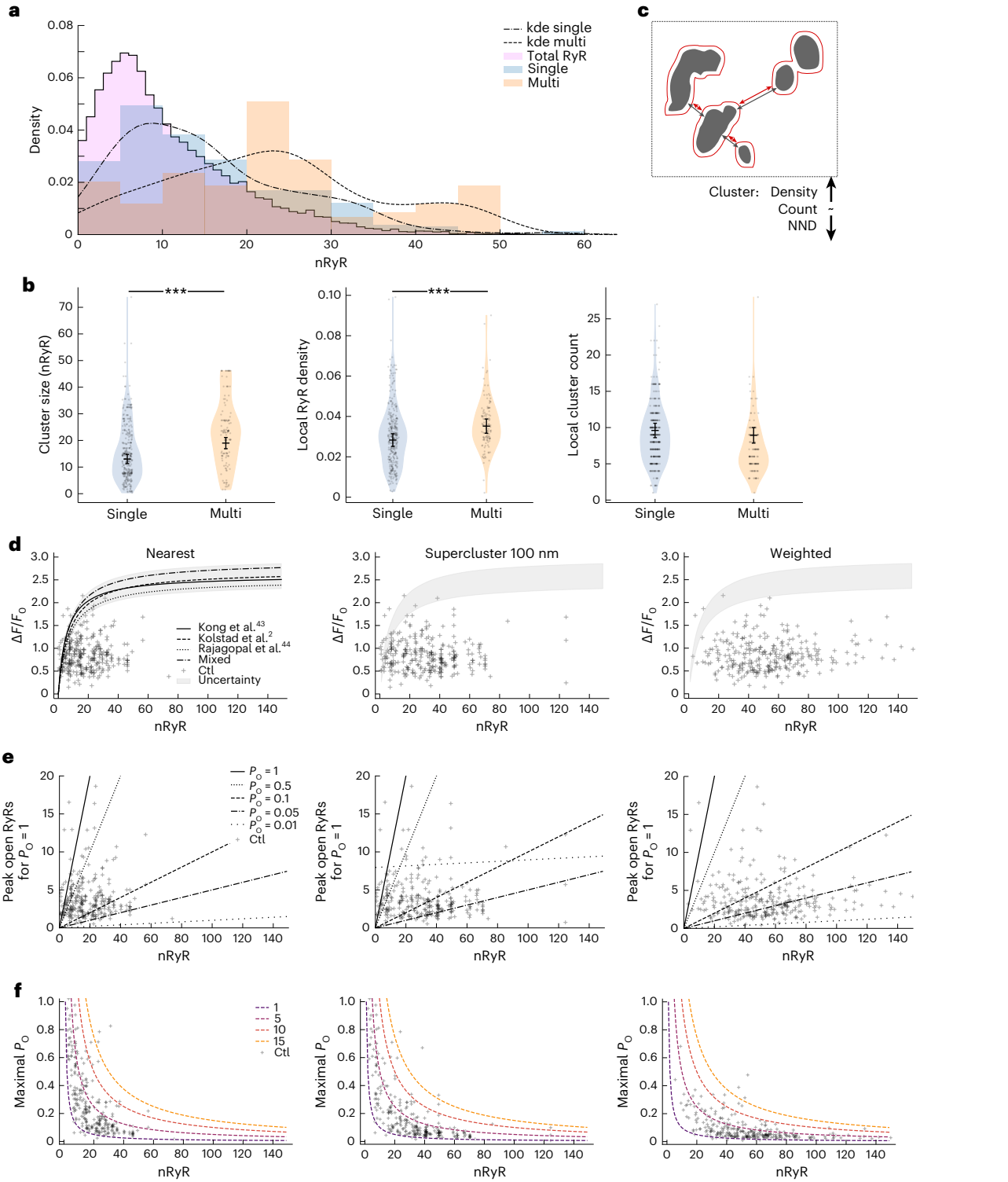

Fig. 4 | Quantitative analysis of Ca^{2+} release sites. a, Measurements of nearest RyR cluster sizes revealed that single-release sparks (blue) generally mapped to smaller clusters than multiple-release sparks (orange). Kernel density estimates (kde) are shown as black lines. The overall distribution of RyR cluster size measurements is illustrated in pink. **b**, Multirelease sparks were tracked to regions of the cell with larger nearest clusters (left) and higher RyR density (weighted RyR measurements based on proximity, center). The mean number of local RyR clusters was similar for the two types of sparks (right). Data are presented as mean ± s.e.m. Differences between groups were tested with two-tailed linear mixed models with Tukey post hoc correction for multiple comparisons. $^{***}P < 0.001$. *P* values: cluster size = 4.57×10^{-5}, local RyR density = 4.3×10^{-4}, local cluster count = 0.1748. For *n* values, see Source data. **c**, Proposed schematic showing that multirelease sparks are most likely to be generated at sites with large and/or tightly packed RyR clusters with short nearest-neighbor distances (NND). **d**, Mathematical modeling predicted the maximal spark amplitude based on the underlying RyR cluster size, assuming all channels open (left). Four models were employed (shaded region 2 s.d. of uncertainty), and experimental measurements of spark magnitude and nearest RyR cluster sizes were superimposed. Comparison was made with correlation of sparks to local RyR 'superclusters' (middle, that is RyRs in clusters within 100 nm) and weighted RyR density (right). **e**, Using the model, the number of peak open RyRs was estimated for each recorded Ca^{2+} spark, and compared with the size of the underlying RyR cluster, supercluster or weighted RyR density. **f**, Estimated maximal RyR P_o for each spark, as a function of contributing RyR arrangement.

https://doi.org/10.1038/s44161-022-00199-2

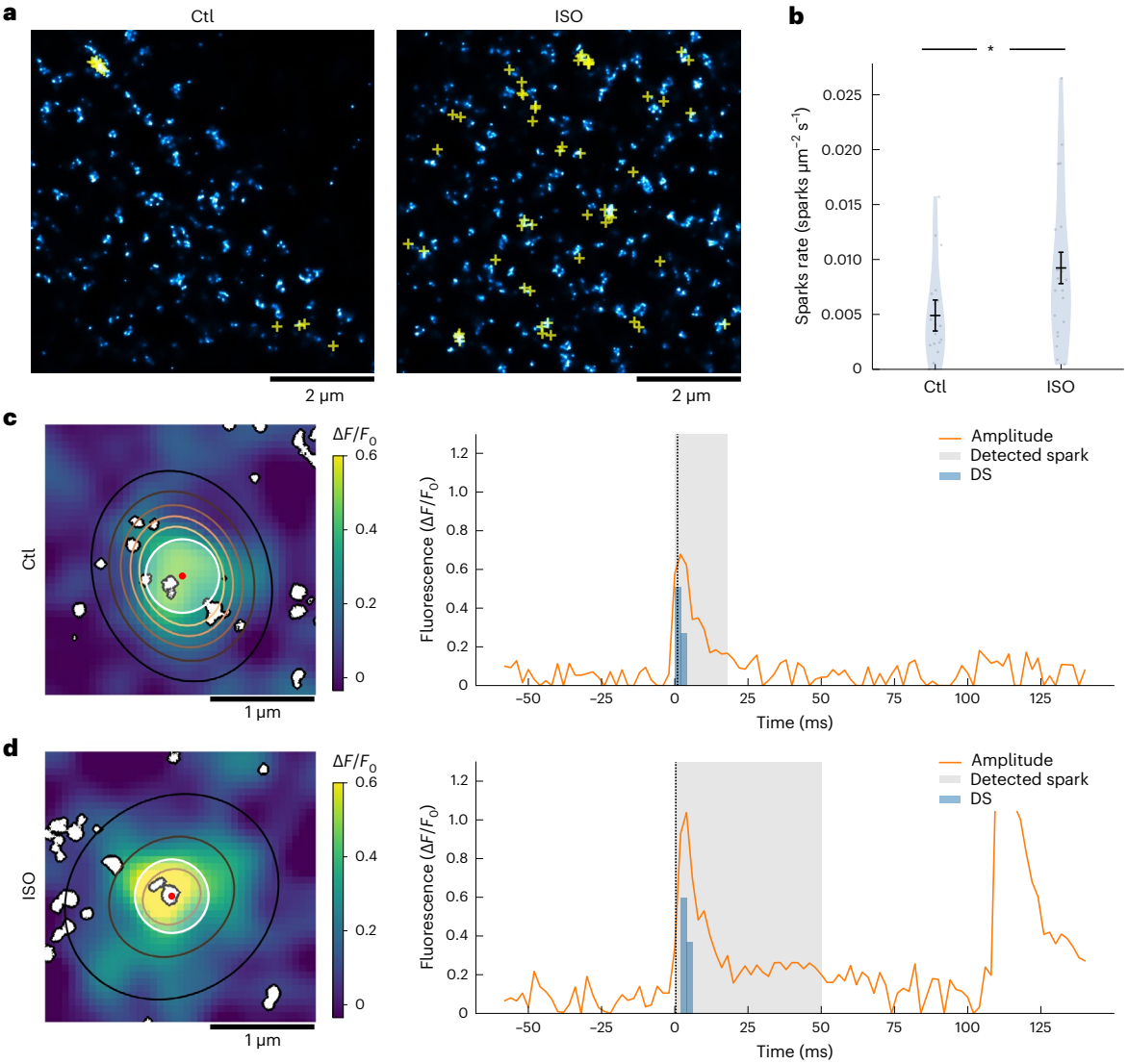

Fig. 5 | Mapping of Ca^{2+} sparks origins during β-adrenergic stimulation. **a**, Correlative Ca^{2+} and RyR imaging in Ctl and ISO-treated cardiomyocytes, with spark locations marked with yellow crosses. **b**, Despite markedly increased spark frequency during ISO stimulation, the majority of Ca^{2+} sparks continued to be superimposed on RyR clusters (79% within 300 nm for Ctl, versus 83% in ISO). Data are presented as mean ± s.e.m. Differences between groups were tested with two-tailed linear mixed models with Tukey post hoc correction for multiple comparisons. $^{*}P < 0.05$. *P* value for spark rate = 0.0291. For *n* values, see Source data. **c**,**d**, Representative DS Ca^{2+} sparks during Ctl (**c**) and ISO treatment (**d**) are illustrated with Ca^{2+}-RyR mapping (left), with spark centroids indicated by red dots and localization uncertainty illustrated by surrounding white circles. Overall spark time courses are shown at the right. Both example sparks are single-release events. DS Ca^{2+} release (blue bars) was larger during ISO, resulting in larger amplitude Ca^{2+} sparks. The dashed line indicates the time point for the Ca^{2+}-RyR overlay, and the duration of spark detection is shown in gray.

with single-release events, multirelease sparks originated at areas with higher RyR density (center panels in Fig. 4b and Extended Data Fig. 7b). However, the number of local RyR clusters was similar for these two types of events (right panels). This implies a closer edge-to-edge distance for clusters initiating multirelease events, as illustrated schematically in Fig. 4c. Thus, multirelease sparks are most likely to be generated at RyR 'hot-spots', where there are large and/or closely spaced RyR clusters which facilitate saltatory Ca^{2+} release.

With assistance from mathematical modeling, we next related the magnitude of each Ca^{2+} release event to the size of the source RyR cluster. Experimental data were interrogated using the 'sticky cluster' mathematical model[13], to estimate the maximal amplitude of a spark that could be generated by a given cluster size, assuming that all RyRs open. Performing the simulations with different literature values describing intracellular Ca^{2+} buffers (see Supplementary Table 2) produced a family of similar curves (Fig. 4d). The logarithmic shape of these relationships is primarily linked to local SR depletion, which limits Ca^{2+} spark amplitude as a larger number of RyRs open[23]. Experimental data were then superimposed, with recorded spark amplitude first plotted as a function of nearest RyR cluster size (Fig. 4d). This presentation indicated that for a given cluster size, the amplitude of the generated Ca^{2+} spark is highly variable, consistent with the idea that any subset of the constituent RyRs may open. Interestingly, even when the expected uncertainty of experimental spark measurement was accounted for (shaded region), we observed that 6% of data points were not constrained by the maximal amplitude curve. However, counting RyRs located within a local 'Ca^{2+} release unit' or 'supercluster' (summation of clusters within 100 nm (ref. [22]; Fig. 4d, center panel), or using locally weighted RyR counts (right panel) allowed the experimental data to be better constrained (5%, 100 nm super cluster, and 1.4%, weighted distance, respectively). Similar results were obtained assuming looser RyR packing (Extended Data Fig. 7c).

This finding suggests that even for defined 'single-release' events, there is likely summated Ca^{2+} release from nearby sites which occurs too rapidly and too locally to allow experimental detection.

We next employed the modeled relationship between RyR number and spark magnitude to predict the maximum number of simultaneously open RyRs that could underlie each experimentally recorded Ca^{2+} spark. These values are plotted paired with corresponding RyR counts, based on the nearest cluster, 100 nm supercluster or weighted RyR density (Fig. 4e). This calibration revealed that Ca^{2+} sparks rarely recruit the full regiment of local RyRs simultaneously, suggesting that channel open probability (P_O) is low. Indeed, using RyR counts at the nearest cluster, the average RyR P_O at the peak of the Ca^{2+} spark was estimated to be only 0.42 ± 0.044, with 73% of values falling between P_O = 0.05 and 0.5 (Fig. 4e, left panel, lines indicated). Using local supercluster or weighted RyR counts of channels which may participate in each spark, produced even lower P_O estimates (0.33 ± 0.043 and 0.11 ± 0.013, respectively). Furthermore, peak P_O was observed to be negatively correlated with cluster size, indicating that in large clusters only very small fractions of RyRs open simultaneously (Fig. 4f; see similar values in Extended Data Fig. 7e assuming looser RyR packing). Overall, we estimate that for the majority of sparks, only between one and five RyRs are simultaneously open at the spark peak.

Regulation of Ca^{2+} release by β-adrenergic stimulation

We next employed our developed methods to assess the effects of acute β-adrenergic stimulation on RyR activity (Fig. 5a). As expected, isoproterenol (ISO) treatment resulted in significantly higher spark frequency (Fig. 5b), although the proportion of events successfully correlated with local RyR clusters remained similar to control (Ctl) conditions (83% versus 79%, respectively). Representative examples of these correlations are presented in Fig. 5c,d, alongside the accompanying Ca^{2+} spark profiles. Interestingly, although ISO treatment increased spark frequency, the proportion of multirelease sparks remained similar to Ctl conditions (Fig. 6a). The movement of the spark centroid (radius of gyration) that occurred during multirelease sparks was also unchanged during ISO, and remained markedly larger than the displacement observed during single-release sparks (Fig. 6b). However, DS release events were significantly larger during ISO treatment, as illustrated by representative plots (Fig. 5c,d) and mean data (Fig. 6c). This observation held true for single- and multirelease sparks, resulting in both types of events showing larger overall spark magnitudes in ISO than Ctl. In the case of multirelease sparks, the spatiotemporal summation of consecutive Ca^{2+} releases during ISO continued to produce larger, longer-lasting sparks than those arising from single-release events (Fig. 6d–f).

To interrogate the mechanism for larger Ca^{2+} release events during ISO, we again employed the mathematical model to link the magnitude of Ca^{2+} release to the size of the source RyR cluster(s). Experimental data were superimposed on the modeled relationship between spark magnitude and local RyR count, assuming that all RyRs open (Fig. 6g). In ISO-treated cells, a greater proportion of sparks appeared near this theoretical maximum than in Ctl. Indeed, overall spark magnitudes were right-shifted towards larger values in ISO (Fig. 6h). Calibrating these values to estimate the maximum number of open RyRs during the spark peak showed a similar skewing towards greater RyR P_O in ISO than Ctl (Fig. 6i), consistent with expected increases in SR Ca^{2+} content and RyR phosphorylation. Taken together, these data indicate that while β-adrenergic stimulation augments Ca^{2+} release by increasing RyR P_O, this increased cooperativity remains very local, without more frequent traveling of Ca^{2+} release between distinct RyR clusters.

Regulation of Ca^{2+} release at internal sites

As our work thus far has investigated spark generation at the cell surface, we next examined whether disparate RyR clusters similarly collaborate to generate Ca^{2+} sparks at internal sites (Fig. 7a). Paralleling cell surface analyses, we observed that 17 ± 6% of sparks recorded at internal sites were multirelease events. These multirelease sparks again exhibited greater movement during their time course than single-release events (radius of gyration, Fig. 7b). Indeed, multirelease sparks recorded within the interior tended to exhibit greater displacement than those on the cell surface (550 ± 77 versus 372 ± 22 nm, P = 0.08), likely reflecting a more complex arrangement of RyR clusters within internal Ca^{2+} release units[9]. As on the cell surface, the summation of multireleases resulted in overall Ca^{2+} sparks that tended to be larger and with slower kinetics than single-release events (Fig. 7c–e).

Similar to observations made on the cell surface, acute ISO treatment increased spark rate within the cell interior (Fig. 7a,f), but not the proportion of multirelease events (ISO 8 ± 4% versus control 17 ± 6%, P = 0.40) or the radius of gyration of these events (Fig. 7b). Comparable effects of ISO were observed in recordings made within the interior of wild-type cells (Extended Data Fig. 8). Paralleling observations made on the cell surface, internal Ca^{2+} spark magnitudes tended to be larger during ISO stimulation, and multirelease sparks larger and slower than their single-release counterparts (Fig. 7c–f). The mean size of RyR clusters was unaltered by ISO treatment (Fig. 7g). These findings support that, as on the cell surface, Ca^{2+} release from internal RyRs is stimulated by β-adrenergic stimulation without augmenting the likelihood that nearby RyR clusters 'collaborate' to generate Ca^{2+} sparks (that is, with distinct, summating release events).

HF promotes RyR dispersion and traveling sparks

Finally, we examined whether RyR collaboration during spark generation is altered during HF. Cardiomyocytes from postinfarction, failing PA-RFP mice were compared with sham-operated controls. Animal data are presented in Supplementary Table 3. Recordings within the cell interior revealed that overall Ca^{2+} spark frequency was not significantly increased in failing cardiomyocytes (0.0053 ± 0.0007 sparks μm^{-2} s^{-1} versus 0.0036 ± 0.0006 sparks μm^{-2} s^{-1} in Sham; P = 0.136; Fig. 8a). However, failing cells exhibited an increased fraction of multirelease events (0.460 ± 0.049 versus 0.286 ± 0.049 in Sham, P < 0.05; Fig. 8b). In agreement with observations in healthy cardiomyocytes, multirelease sparks recorded in HF cells continued to propagate further and were larger and slower than their single-release counterparts (Fig. 8b). As we have observed that multirelease sparks are favored by a higher density and closer spacing of RyR clusters (Fig. 4a–c), we hypothesized that there is critical reorganization of RyRs in failing cardiomyocytes. Indeed, dSTORM imaging revealed RyR 'dispersion' in failing cells, with fragmentation of clusters into more numerous, smaller units (Fig. 8c). Quantitative analysis confirmed that although overall RyR density was unchanged during HF, mean cluster size was reduced, while cluster density increased (Fig. 8d). A similar trend was observed in PALM data from live cells, although the slightly lower resolution of this technique (~45 nm versus ~20 nm in dSTORM, Extended Data Fig. 3) was insufficient to detect significant changes (Extended Data Fig. 9). The observed spatial reorganization of RyRs in failing mouse cells is in agreement with our previous observations in HF rats[2,16], and supports that RyR cluster dispersion enables an increased appearance of multirelease, traveling sparks, which slows overall Ca^{2+} release in this condition.

Discussion

In this study, we have demonstrated methods for correlating RyR organization and function in live cardiomyocytes. By implementing signal processing methods to isolate only newly released Ca^{2+}, we performed a detailed assessment of Ca^{2+} release origins, showing that many sparks consist of distinct release events with propagation between multiple RyR clusters. Multiple-release sparks can move up to 1000 nm during their time course, may involve RyRs sharing the same jSR or neighboring jSR, and preferentially occur at sites with larger RyR cluster sizes, higher RyR density and/or shorter distances between neighboring RyR clusters. Our analyses further showed that although any number of RyRs

https://doi.org/10.1038/s44161-022-00199-2

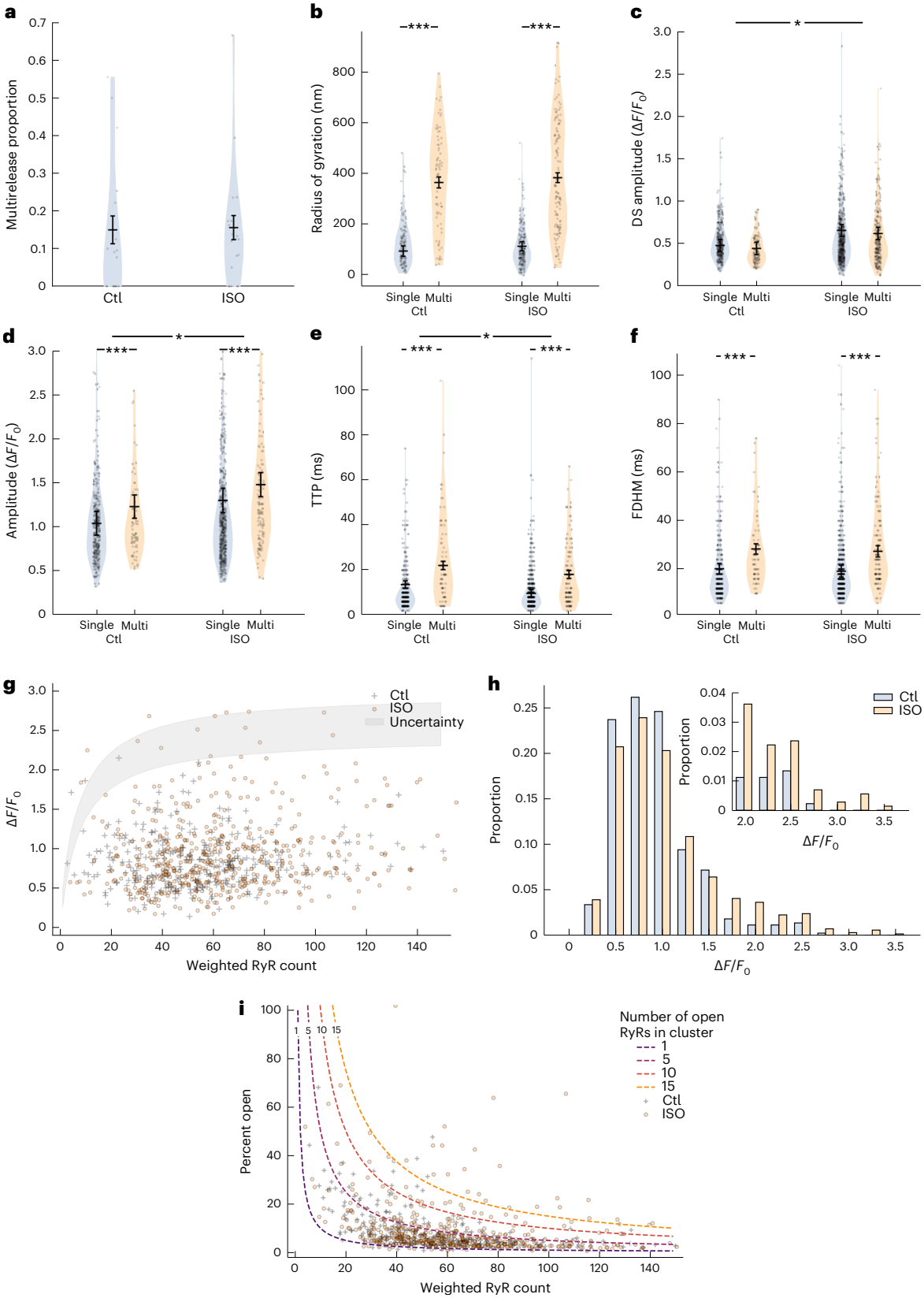

Fig. 6 | β-adrenergic stimulation increases RyR recruitment during Ca^{2+} sparks. a,**b**, ISO treatment did not alter the proportion of total sparks which exhibit multiple releases (**a**) or their travel distance (**b**). **c**–**f**, However, the amplitude of each DS Ca^{2+} release event was larger during ISO (**c**), resulting in larger overall Ca^{2+} sparks (**d**), without increasing spark time to peak (**e**) or duration (**f**). Data are presented as mean ± s.e.m. Differences between groups were tested with two-tailed linear mixed models with Tukey post hoc correction for multiple comparisons. $^{*}P < 0.05$, $^{**}P < 0.01$, $^{***}P < 0.001$. Please refer to Source data for exact *P* values and *n* values. **g**, Experimentally measured spark amplitudes and corresponding weighted RyR counts were plotted, together with the theoretical maximal spark amplitude curve (see also Fig. 4d). **h**, ISO produced an upward shift, as sparks skewing toward larger amplitudes. **i**, Using the mathematical model to calibrate the number of open RyRs during each spark revealed a similar skewing towards larger values during ISO treatment.

https://doi.org/10.1038/s44161-022-00199-2

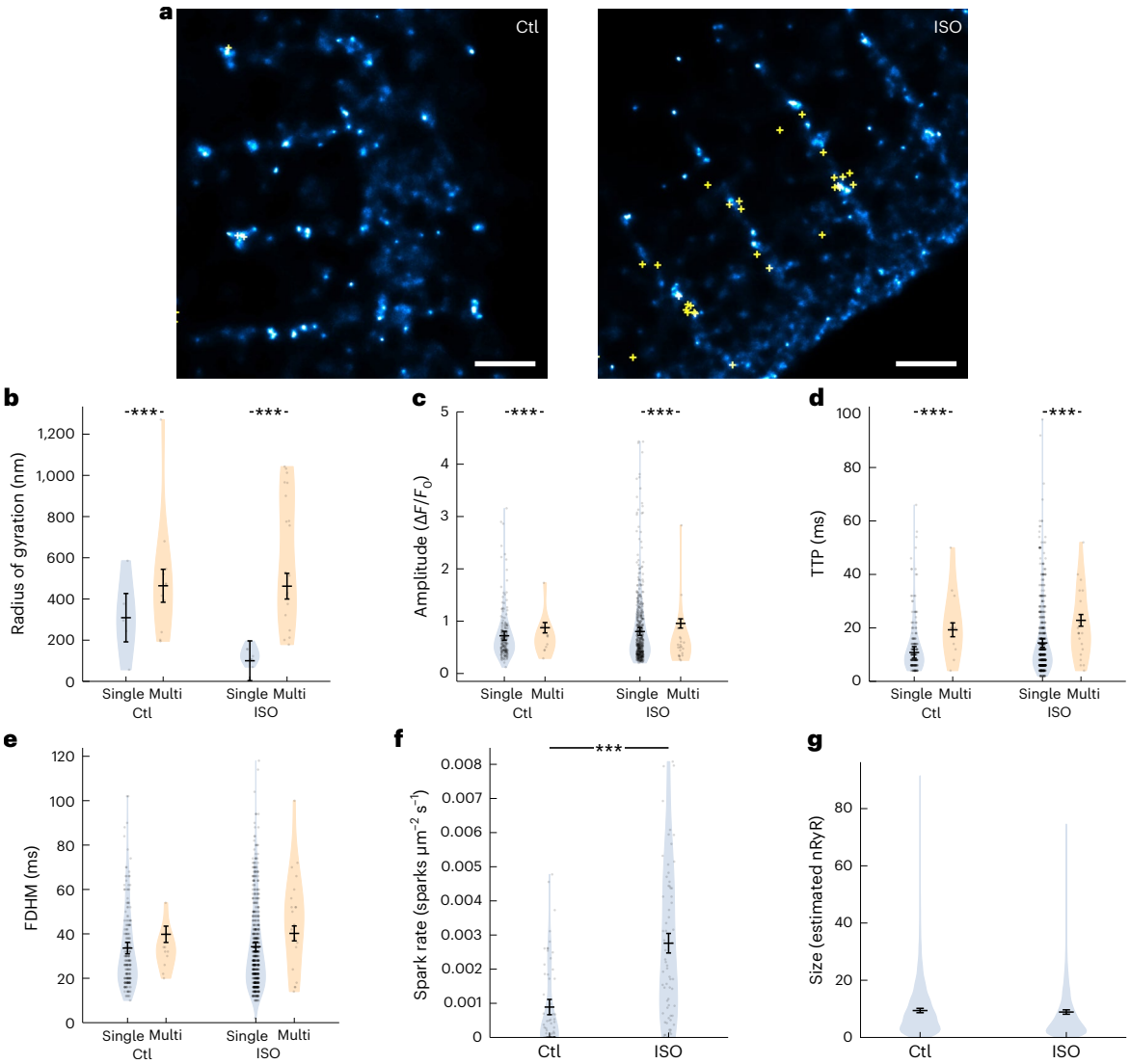

Fig. 7 | Regulation of Ca^{2+} release at internal sites. a, Using highly inclined and laminated optical sheet imaging, correlative Ca^{2+} and RyR imaging was performed within the cell interior. Scale bars, 800 nm. **b**–**e**, As observed on the cell surface (see previous figures), multirelease Ca^{2+} sparks at internal sites exhibited greater movement than single-release events (**b**), and tended to be larger (**c**), with slower kinetics (**d**,**e**). **f**,**g**, ISO treatment markedly increased spark rate (**f**), but not the proportional occurrence of multirelease sparks (see main text) or RyR cluster sizes (**g**, estimated by tight RyR packing within thresholded 2D area). Data are presented as mean ± s.e.m. Differences between groups were tested with two-tailed linear mixed models with Tukey post hoc correction for multiple comparisons. $^{*}P < 0.05$, $^{**}P < 0.01$, $^{***}P < 0.001$. Please refer to Source data for exact *P* values and *n* values.

within a cluster may open during a Ca^{2+} spark, RyR P_O is generally low in intact cardiomyocytes. Indeed, during the peak of a typical spark, only a minor fraction of RyRs in a cluster are simultaneously open. We show that intracluster RyR recruitment is enhanced during β-adrenergic stimulation, which allows generation of larger, albeit predominantly local, release events. In contrast, traveling sparks are favored during heart failure due to dispersion of RyR clusters into smaller, more numerous groupings. Thus, RyRs generate Ca^{2+} sparks in a complex fashion, and the propensity for multicluster release events is regulated by the physical positioning of the channels.

The detection of multirelease Ca^{2+} sparks in this study has been made possible by two features of our imaging and analysis protocols. First, we recorded Ca^{2+} signals at a frame time of 2 ms, a speed notably faster than the 10–100 ms frame times used in most previous studies that have performed 2D spatial imaging[3,24,25]. This enabled the extraction of critical temporal data on par with 1D line-scan recordings of sparks, although our simulated line-scans showed how 1D imaging can easily result in failed detection or mischaracterization of multirelease events (Fig. 2d). A second critical feature of our imaging and analysis pipeline is the application of DS[20,26]. By revealing only the 'new' Ca^{2+} released in each frame, these analyses unveiled the mobile nature of Ca^{2+} sparks, which can be obscured when multiple releases are temporally superimposed (Fig. 3b).

For linking Ca^{2+} release events to individual RyR clusters, we relied on PALM imaging, which yielded a localization precision comparable to dSTORM imaging in fixed cells (Extended Data Fig. 3; localization precision ~20 nm versus 5–15 nm). Although others have attempted to link super-resolution-defined RyR locations in fixed cells to Ca^{2+} sparks recorded before fixation[25], it should be noted that multiday fixation, labeling and imaging protocols offer considerable opportunity for perturbations of cell geometry and alignment. Furthermore, recent data indicate that the RyRs themselves can also be repositioned[8,14] in a time-dependent manner[16,18]. In contrast, our live-cell imaging protocol enables rapid imaging of Ca^{2+} and RyRs (20 s and 5 min, respectively), and PALM imaging avoids issues of nonspecific secondary antibody labeling endemic to techniques like dSTORM (Extended Data Fig. 3).

https://doi.org/10.1038/s44161-022-00199-2

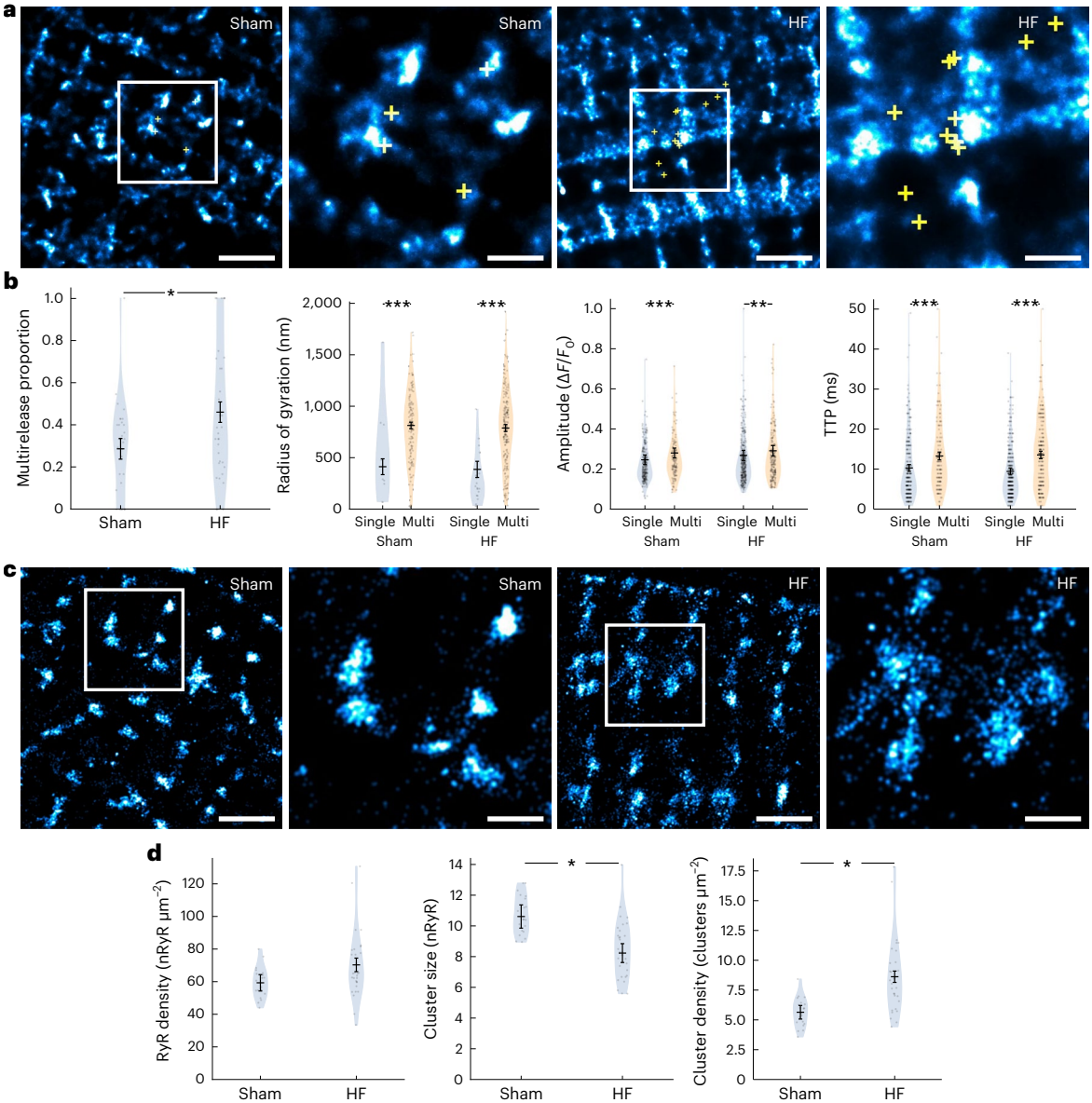

Fig. 8 | RyR cluster dispersion during heart failure promotes multirelease, traveling sparks. a, Correlative imaging of Ca^{2+} and RyRs within the interior of cardiomyocytes isolated from mice with postinfarction HF. Comparison was made with sham-operated controls (Sham). **b**, Failing cells exhibited an increased proportion of multirelease sparks. As in Sham, multirelease sparks observed in failing cells traveled further, and were larger and slower than single-release events. **c**, **d**, dSTORM imaging revealed marked 'dispersion' of RyRs in HF (**c**), resulting in the appearance of smaller but more numerous clusters, and no change in overall RyR density (**d**). Scale bars in **a** and **c**, 1.6 µm in zoom-outs, 750 nm in enlargements. Data in **b** and **d** are presented as mean ± s.e.m. Differences between groups were tested with two-tailed linear mixed models with Tukey post hoc correction for multiple comparisons. $^{*}P < 0.05$, $^{**}P < 0.01$, $^{***}P < 0.001$. Please refer to Source data for exact *P* values and *n* values.

Although we were unable to match a minority of Ca^{2+} sparks to their origins, we expect that this discrepancy likely resulted from detection of Ca^{2+} from release sites outside the imaging plane. Alternatively, incomplete photoactivation and quantification of RyR positions could occur in our PALM experiments, although the similarity of the obtained cluster sizes with dSTORM-based measurements (Fig. 1b) suggests that this is not a frequent occurrence.

We observed that traveling sparks tend to arise from areas of the cell with higher RyR density, where clusters are tightly packed (Fig. 4a–c). Thus, our data directly support that multicluster 'Ca^{2+} release units' or 'superclusters' of RyRs can collaboratively generate Ca^{2+} sparks; a concept previously proposed based on mathematical modeling[2,4,13,27]. Furthermore, 'dispersed' RyR configurations in failing cells provide a greater opportunity for the generation of multirelease, traveling sparks (Fig. 8). This observation corroborates previous modeling work linking 'slow' Ca^{2+} sparks to dispersed RyR configurations in HF[2,16,28] and atrial fibrillation[17]. Notably, traveling sparks are not merely chance occurrences of independent sparks occurring nearly simultaneously. Indeed, our calculations show that the probability of independent events exhibiting spatiotemporal superimposition should be at most ~3% (Methods). Thus, in the vast majority of cases, follow-up release events are the direct consequence of the initial release. Interestingly, the propagation of Ca^{2+} release during multirelease sparks did not seem to follow any predefined pattern, such as triggering of the nearest adjacent RyR clusters or even clusters within the same jSR. Thus, the ability of nearby RyR clusters to collaboratively generate Ca^{2+} sparks may rather be determined by posttranslational modifications which locally alter RyR

Ca^{2+} sensitivity[14,29], or subcellular structures such as mitochondria or t-tubules which impede Ca^{2+} propagation between some sites[30].

While multirelease sparks occur preferentially at sites with large and/or tightly packed RyR clusters, single-release spark parameters show very little dependence on RyR organization. In fact, when the centroid of each individual release was tracked to the nearest RyR cluster, we observed that for a given cluster size there was large variation in the accompanying spark amplitude (Fig. 4d). With support from mathematical modeling (Extended Data Fig. 5), this observation suggests that for a given cluster size, any number of the constituent RyRs may open. Notably, even when we simulate all RyRs within the Ca^{2+} release unit opening simultaneously, there is only a correlation between cluster and spark size when the clusters are quite small. This relationship quickly disappears when the number of RyRs exceeds ~10, and the curve saturates. This finding is consistent with the 'induction decay' model[23,31], where spark magnitude is restricted when larger numbers of RyRs open, as jSR volume is depleted.

How many sparks open during a typical Ca^{2+} spark? Historically, estimates have varied considerably. Indeed, it was initially proposed that sparks result from the opening of single RyRs "or a small number of channels acting in concert"[1]. However, later estimates were much larger as it was proposed that dyads were densely packed with >100 RyRs[32], with all channels opening during a spark. Our present work supports a growing appreciation that RyR clusters (and Ca^{2+} release unit groupings of RyR clusters) are far smaller than these earlier estimates[9,22], and that only a fraction of channels are simultaneously open[23]. While we estimate that between one and five RyRs are concurrently open during a typical spark (Fig. 4f), such approximations are dependent on the accuracy of the mathematical model. Other models (for example, ref. [23]), yield a relationship between spark magnitude and RyR number that saturates at smaller spark sizes, which would produce somewhat larger estimates.

Given the cooperative nature of RyR cluster activity under baseline conditions, we were somewhat surprised that these functional associations were not more dramatically altered during acute β-adrenergic stimulation. Although individual release events tended to be larger during ISO (Figs. 6c and 7c), consistent with expected increases in SR Ca^{2+} content, RyR phosphorylation/sensitivity and RyR openings (Fig. 6i), the magnitude of release continued to be well constrained by modeling (Fig. 6g). Furthermore, the proportion of traveling sparks was unaltered during ISO, indicating that Ca^{2+} release remains a controlled and local event. Nevertheless, it should be remembered that the number of spontaneous Ca^{2+} sparks increases during β-adrenergic stimulation (Figs. 5b and 7f), and therefore the absolute number of traveling sparks (and waves[33]) increases. Importantly, more prolonged β-adrenergic stimulation would likely have different effects on RyR collaboration, as chronic ISO treatment disperses RyR clusters in a manner resembling changes in HF[16].

The PALM imaging techniques presently employed have enabled RyR imaging at a resolution beyond what is possible in diffraction-limited approaches in live cells (~45 nm versus ~250 nm) (ref. [3]). However, the resolution attained by PALM remains somewhat below the actual dimensions of the RyR itself (30 x 30 nm). Thus, some errors in quantifying absolute numbers of RyRs within each cluster are inevitable. However, such inaccuracies have been minimized by performing our initial studies at the cell surface, where the relatively flat arrangement of RyRs avoids complications that arise when RyRs are axially superimposed[9]. We have addressed the critical issue of RyR packing within each imaged cluster by assuming a tight, grid-like arrangement of RyRs[9,22], or a looser arrangement of RyRs reported by the higher resolution DNA-PAINT technique (~5 nm (ref. [10]), Extended Data Fig. 7). Notably, although DNA-PAINT requires fixed cells, similar event counting-based principles for extracting absolute protein quantities can theoretically also be performed using PALM imaging[34,35]. In a preliminary analysis, we have observed that event counts in our PALM experiments are in fact correlated with area-based measures of cluster sizes (Extended Data Fig. 10).

In conclusion, the present work has provided insight into the complexity of RyR function. Our data show that Ca^{2+} sparks can comprise single- or multiple-release events, originating from highly variable numbers of RyRs within the same cluster or nearby clusters. Although RyR P_O is generally low, RyR recruitment is malleable by stimuli such as β-adrenergic stimulation, which allows more concerted opening of nearby channels. Such local constraints on Ca^{2+} release are mitigated during HF, as dispersion of RyR clusters into smaller, more numerous groupings allows for the more frequent occurrence of 'traveling' sparks. Thus, while RyR collaboration is locally malleable in healthy cells to allow fine-tuning of Ca^{2+} release and contraction, this tight control is lost in disease.

Methods

All animal protocols were performed in accordance with the Norwegian Animal Welfare Act and NIH Guidelines (NIH publication No. 85-23, revised 2011) and were approved by the Norwegian Food Safety Authority (permit number 8951).

Creation of PA-RFP RyR mouse

A genetically modified mouse on C57BL6/6N background was created by Cyagen Biosciences. PA-TagRFP was inserted after T1365, within exon 31 of the *Ryr2* gene on chromosome 13 (genebank NM_023868.2, ensembl ENSMUSG00000021313), placing the fluorophore within subdomain 6 of the 'clamp' region of the protein. The targeting strategy (illustrated in Extended Data Fig. 1a) was achieved by homologous recombination via standard neomycin cassette gene insertion and selection. Linearized insertion vectors were combined into cells by electroporation with 16 candidate embryonic stem cells. These cells were then developed and successful recombinants were selected for using neomycin resistance. The selected embryos were allowed to mature and the neomycin resistance gene was removed by crossing with Cre^+ mice.

To minimize possible steric hindrance from the attached RFP, the sequence was flanked by 10-residue and 9-residue glycine-rich linkers on the 5′ and 3′ sides, respectively. This approach was modeled on previous work, which showed that a GFP insertion at this approximate site did not disrupt RyR function or result in any deviant in vivo phenotype[18]. Our data confirmed that at 8–10 weeks of age, both animal and heart weights were normal in the created PA-RFP RyR mouse (Extended Data Fig. 2a), and that Ca^{2+} transients in isolated cardiomyocytes were also unchanged from age-matched C57BL6/6N wild-type (Extended Data Fig. 2b,c). In all further experiments, 8–10-week-old mice of both sexes were used, apart from those used following surgery, which were 13–15 weeks of age (see following section). Animals were housed in a temperature- and humidity- regulated room with a 12 h day/12 h night cycle.

Mouse model of postinfarction HF

After preoperative analgesia with subcutaneous buprenorphine (0.1 mg kg^{-1}), 8–10-week-old animals were anesthetized with 5% isoflurane, intubated and ventilated with a VentElite (Harvard apparatus) using 2% isoflurane and 98% oxygen. Marcaine (1 mg kg^{-1}) was injected at the incision site and hair removed. The incision site was disinfected, and through an anterior thoracotomy, the left anterior descending coronary artery was ligated without exteriorizing the heart[36]. Sham-operated underwent the same procedure without ligation. Surgical incisions were sutured, and the animal observed until resumption of normal activity. Postoperative analgesia was given with buprenorphine. Development of heart failure was verified 5 weeks following infarction surgery using a Vevo 2100 echocardiography imaging system (VisualSonics) and established criteria[37]. Detailed structural and functional assessment was provided by magnetic resonance imaging

on a 9.4 T preclinical MR system, using cine imaging, as previously described[38]. Mean measurements from sham and failing hearts are shown in Supplementary Table 3.

Cardiomyocyte isolation

Single cardiomyocytes were isolated as previously described[39]. Briefly, mice were anesthetized by isoflurane inhalation and euthanized by cervical dislocation. The heart was then rapidly excised and cannulated through the aorta on a constant flow Langendorff perfusion system. The coronaries were first cleared of blood by flushing the heart with 5–10 ml of isolation buffer at 2 ml min^{-1}. This isolation buffer contained (in mM) NaCl 130, KCl 5.4, $MgCl_2$ 0.5, NaH_2PO_4 0.4, HEPES 25 and D-glucose 5.5, and was pH adjusted to 7.4 with NaOH at room temperature (RT). Perfusion was then switched to isolation buffer including 2 mg ml^{-1} collagenase type II (Worthington Biochemical, catalog: LS004176) for 7 min at 2 ml min^{-1}. Following digestion, the heart was cut down from the apparatus, and placed in isolation buffer containing 1 mg ml^{-1} bovine serum albumin, where the left ventricle was diced into chunks. After filtering through 200 µm filter mesh (SEFAR S-TEX PET 200), cardiomyocytes were sedimented and the Ca^{2+} concentration was progressively increased (0.1, 0.2 and 0.5 mM). Isolated cells were used in experiments within 4 h of isolation.

Live-cell Ca^{2+} and PALM imaging

For live-cell imaging, freshly isolated cardiomyocytes were first transferred to HEPES Tyrode's (HT) buffer containing (in mM) 140 NaCl, 5.4 KCl, 1.0 $CaCl_2$, 0.5 $MgCl_2$, 5.0 HEPES, 5.5 glucose and 0.4 NaH_2PO_4, with pH adjusted to 7.4 by NaOH, at RT. After 15 min of equilibration, 200 µl of cells was transferred to the imaging coverslips (MATTEK, Catalog: P35G-0.170-14-C), and incubated with 2 µM of the Ca^{2+}-sensitive dye Cal520-AM (AAT Bioquest Catalog: 21130) for 1 h at RT. Excess HT solution was then removed, and replaced with HT containing 15 mM 2,3-butanedione monoxime (BDM, Sigma Aldrich Catalog: B0753-25G) to prevent cell contraction. In some experiments, cells were exposed to 150 nM ISO for 5 min.

Imaging was performed with a modified Zeiss 710 Elyra system (Carl Zeiss) equipped with a Zeiss alpha apochromat ×63 1.46 NA objective (Model: 420780-9970-000) and a Hamamatsu ORCA-Fusion sCMOS camera (Model: C14440-20UP). HCImage Live software (Hamamatsu, v.4.4.2.7) was used to record raw data for PALM, dSTORM and Ca^{2+} spark measurements. For cell surface images, TIRF imaging was employed, using an illumination angle of 69°. For imaging of Ca^{2+} sparks within the cell interior, we employed highly inclined and laminated optical sheet imaging with a typical illumination angle of 57°. Cells were imaged sequentially, starting with Ca^{2+} recording, where excitation was performed with a 488 nm laser. Laser power was set at ~5 mW power directed at a ~45 µm diameter circle to produce a final power of 7 W mm^{-2}. Ca^{2+}-dependent fluorescence was recorded at 515 nm within a 36 x 18 µm region of the cell, captured at 2 ms integration time for 10,000 images. PALM imaging of RyRs was then initiated, using a 405 nm laser at 0.7 W mm^{-2} for photoactivation, and a 561 nm laser at 40 W mm^{-2} for excitation. For a total acquisition time of 4 min 10 s, 5,000 frames were captured at 50 ms per frame. Acquired PALM image data were processed and rendered using the Python Microscopy Environment (PyME, v.3.6.9, https://python-microscopy.org/).

dSTORM imaging

For dSTORM imaging, coverslips (MATTEK, Catalog: P35G-0.170-14-C) were first coated with poly-L-lysine (Sigma Aldrich Catalog: P8920) by overnight incubation at 4 °C. Next, 200 µl of the cardiomyocyte-containing solution was placed on each coverslip, and cells were allowed to settle for 30 min. The supernatant was then removed, and fixation initiated by addition of 500 µl of 2% PFA for 10 min. Fixation was quenched by replacing PFA with 2 mM glycine solution, and incubating for 1 h at RT. Cells were then permeabilized with 0.1% Triton X-100 for 15 min, washed three times with PBS and blocked using Image-iT FX signal enhancer (Invitrogen Catalog: 136933) for 1 h at RT. Cells were immunolabeled with primary anti-RyR antibody (MA-916 C3-33, ThermoFisher Scientific), at 1:100 dilution in low blocking buffer (2.5% normal goat serum in PBS) overnight at 4 °C. Following three washes with PBS, secondary antibody (F(ab')2-Goat anti-Mouse IgG with Alexa Fluor 647, Catalog: A21237, ThermoFisher Scientific) was added at 1:200 dilution and incubated at RT for 2 h, before a final three washes with PBS.

dSTORM acquisition was carried out using the same apparatus as described for PALM imaging utilizing 642 nm laser illumination at 300 W mm^{-2}, with acquisition recorded for 50 ms per frame over 15,000 frames (total imaging time = 12.5 min). Acquired dSTORM image data were processed and rendered using PyME.

RyR imaging analysis

RyR image data from both PALM and dSTORM imaging modalities were first segmented via local thresholding, implemented by Python's SciPy ndimages library, with a radius of 500 nm. The threshold was set at 100 counts per $µm^2$ above local background. Above-threshold pixels were then counted and divided by the expected RyR density for estimation of RyR number. We calculated these values assuming either tight, grid-like packing of RyRs (RyR area = 900 nm^2; see also refs. [9,12]) or a lower packing density (66% of grid-based values), approximating values reported in recent DNA-PAINT studies[11]. In preliminary analysis, we also demonstrated that event counts in PALM experiments are correlated with the segmented RyR area, using least-squares fitting with a linear function and statistical testing with Pearson's correlation coefficient (Extended Data Fig. 10).

Analysis of Ca^{2+} sparks

Analysis of Ca^{2+} spark data was performed as illustrated by example images in Extended Data Fig. 4. The employed scripts are available at: https://gitlab.com/louch-group/2d-spark-detector.

Background extraction. The sensor A/D offset for the imaging camera (Hamamatsu ORCA-Fusion sCMOS, Model: C14440-20UP) was obtained from the manufacturer's specifications, and subtracted from the raw input image before background extraction. To ensure that Ca^{2+} sparks, waves, and transients were not included in the background estimation, we first processed the input raw image by thresholding for regions with rapid Ca^{2+} fluctuations. To this end, we temporally smoothed data with a Gaussian filter of 20 ms, and calculated the first and second derivatives over time for each imaged pixel in the smoothed image. Time points with deviations greater than the noise values (3 s.d. of the background fluctuation) were then selected with a mask. These masked pixels were removed from the background fitting as they represent nonbackground states. Pixel-wise background extraction was then carried out using the least-squares cubic univariate spline interpolation function found in Python's scipy library, relying on seven predesignated anchor points evenly spaced in time through the recording. The created background map was then subtracted from the raw image. Background and background-subtracted images were then stored for future data processing. These stages of processing are shown for an example recording in Extended Data Fig. 4, with raw, background and background-subtracted images (a, b and c, respectively).

DS. To generate DS images, we employed methods developed by the Lipp group[20]. With these techniques, the Ca^{2+} fluorescence signal in each frame is convolved and its point diffusion structure is utilized to estimate the expected Ca^{2+} signal present in the subsequent frame. Thus, by subtracting this latent Ca^{2+} signal, only the 'new' Ca^{2+} released within the 2 ms frame time is estimated.

Identification of candidate sparks. Ca^{2+} spark detection was carried out in two phases: an initial phase where candidate sparks were identified and a second phase where detailed spark parameters were extracted. For initial detection, data were temporally reduced by down-averaging raw data from 10,000 to 1,000 frames, and each frame was then spatially smoothed with a 2 pixel (130 nm) Gaussian filter. Background noise intensity was estimated by measuring the s.d. of intensity values in each frame. An iterative, five-step thresholding protocol was then utilized to identify intensity peaks between 6 and 10 s.d. above background noise, creating rough 'topographical maps' for each candidate spark region. We then calculated the center of mass for each map to identify its centroid. To validate that initial rough fitting had identified a spark and not noise fluctuation, we applied twin axis Gaussian fitting of a 41 x 41 pixel region of interest (ROI) around the centroid, using the center of mass and peak amplitude as fitting parameters. Centroids unlikely to be sparks were disregarded based on the width of the fitted Gaussian and its amplitude (see Supplementary Table 1). The loose tolerances of this initial filtering protocol primarily served to remove false detections, waves and protowave Ca^{2+} activity. An example of a Ca^{2+} spark identified by initial filtering is presented in Extended Data Fig. 4d.

Refined fitting for confirming spark locations, and assessing spark dimensions. The filtered centroids were next used as references for refining spark identification. Based on each centroid's x, y and t positions, ROIs of 41 × 41 × 100 pixels (2.5 µm × 2.5 µm × 200 ms) were extracted from the background-subtracted and DS images (see frame-by-frame examples in Extended Data Fig. 4e). The ROI for each frame was then passed through two fitting regimes. In initial fitting, images were blurred with a 2-pixel Gaussian filter to reduce the number of false detections due to noise fluctuation. Spark amplitude, width and rotation were then fitted for each frame in the background-subtracted, unfiltered image stacks. Finally, we measured spark parameters as a post hoc analysis during the full spark time course. Criteria and boundary limits for each spark parameter are summarized in Supplementary Table 1. Each final detected and measured spark was stored as an image stack, together with a file listing its measured parameters.

Estimation of multirelease spark probability due to chance. When analyzing multirelease sparks, it was necessary to consider the probability that two sparks randomly appear within a ROI in a certain time frame. To this end, we estimated the number of sparks that could occur in the same 2 × 2 µm area where the first spark was detected, within Δt = 50 ms (that is, double the full-duration half-maximum (FDHM) found for multirelease sparks, Fig. 2c). Taking into account that the measured average spark rate was 0.09 and 0.16 sparks $\mu m^{-2}\ s^{-1}$ in control and ISO experiments, respectively (Fig. 5b), we calculated that 0.018 and 0.033 sparks could be expected to occur after the first release was observed. Thus, under Ctl and ISO conditions, there is respectively a 1.8% and 3.3% chance that the second observed Ca^{2+} release occurs merely by chance. It is intuitive that with an increase of the spark frequency during ISO, there is a higher probability that distinct Ca^{2+} sparks are mistakenly identified as a single multirelease spark. However, experimental data (Fig. 6a) showed only a ~0.7% increase in the proportion of multirelease sparks during ISO, indicating that the probability for observing multisparks is actually slightly lower than estimated.

Correlation of Ca^{2+} spark and RyR positions

With sequential imaging of Ca^{2+} and RyRs in our experiments, a chromatic shift is expected to produce random misalignment between the two color channels. To account for this, we first employed fluorescent beads to map fixed chromatic shift before experimental acquisition. Following imaging, the mechanical shift caused by switching filters was manually corrected by aligning the RyR image data with images of the SR, obtained from the background signal measured during background subtraction processing (Extended Data Fig. 4f,g). The required residual shift was typically quite small, and indeed the maximal required shift distance was 300 nm. These shift data were supplied to our alignment script, to correct Ca^{2+} spark centroid positions obtained from the spark detector. Each spark location was then correlated to RyR positions, using the thresholded mask data from the segmented PALM images (Extended Data Fig. 4h,i). Several measurements were then performed:

Nearest RyR cluster. By assigning unique labels to each RyR cluster, spark centroids were traced to the nearest RyR using Python's skimage and scipy libraries.

Superclusters. RyR superclusters corresponding to each spark centroid were determined by first identifying the nearest RyR (as above), and then dilating the segmented RyR mask by 50 nm to gather clusters localized within 100 nm. Neighboring clusters which were conjoined during this dilation were identified using the nearest-neighbor calculation.

Weighted contribution. Finally, we examined the RyR density at each spark's origin, within an area defined by the 2D fitted spark Gaussian (centroid position ± 2 s.d.). All segmented pixels within this region were then considered to contribute to the resultant spark, but this contribution was weighted toward RyRs closer to the spark center. This weighting was based upon the intensity of the Ca^{2+} signal (from the fitted spark) at the receptor with the highest Ca^{2+} concentration (that is the center of the spark) assigned a value of 1.

Mathematical modeling of Ca^{2+} sparks

To simulate the spatiotemporal evolution of Ca^{2+} sparks, we first used the previously published 'sticky cluster' model[13,40] to calculate RyR Ca^{2+} flux from the SR to the cytosol. The calculated flux was then used as an input for a reaction-diffusion model where diffusion and Ca^{2+} binding to different Ca^{2+} buffers were accounted for. Finally, the resulting Ca^{2+} spark was convolved with a TIRF point-spread function. The source code employed for modeling is available at https://gitlab.com/louch-group/sparks-simulator.

Sticky cluster model. Extended Data Fig. 5a (left panel) shows a diagram of the employed 'sticky cluster' model. Equations and parameter values were set as in Ramay et al.[40], with the exception that the number of RyRs in a cluster was varied to derive the relationship between cluster size and maximal Ca^{2+}-dependent fluorescence. We specifically employed cluster sizes of 2, 5, 10, 15, 20, 25, 30 and 50 RyRs, and simulations were carried out over a 25 ms time frame. Simulations were initiated with all RyR closed for a period of 1 ms, after which one RyR in the cluster was set to the open state. The resulting increase in dyadic Ca^{2+} concentration in turn increased the transition rate from the closed state to open for other RyRs in the cluster. An example series of simulations is presented in the middle panel of Extended Data Fig. 5a, illustrating RyR opening dynamics for a cluster containing 10 RyRs. As the opening of RyRs is stochastic, Ca^{2+} efflux from the SR can vary considerably between simulations (Extended Data Fig. 5a, right panel). Therefore, for further analysis, we determined the average maximal Ca^{2+} flux by selecting from 500 simulation runs where all RyRs in the cluster opened, and the time to peak release occurred within the first quartile of measurements. An example of this average flux (J_{efflux}) is shown in red in the right panel of Extended Data Fig. 5a.

The model was implemented in Python. Ordinary differential equations were solved using the 'lsoda' integration method implemented in the SciPy.integrate.ode function, which automatically switches between stiff and non-stiff integration routines. The maximum time step for integration was set to 1 µs.

Reaction-diffusion model. The reaction-diffusion model illustrated in Extended Data Fig. 5b (left panel) was employed to simulate the spatiotemporal development of Ca^{2+} sparks based on the calculated average Ca^{2+} efflux. The model consisted of a set of partial and ordinary differential equations to calculate Ca^{2+} bound and free cytosolic [Ca^{2+}]. Buffered [Ca^{2+}] was calculated using the following equation:

$$\frac{\partial B}{\partial t} = D_B \nabla^2 B + J_B$$

where B is Ca^{2+} bound buffer concentration, D_B is the respective buffer diffusion coefficient and J_B is the corresponding buffer's relative flux. Four Ca^{2+} buffers were included: the Ca^{2+}-sensitive dye, ATP, calmodulin and troponin. Parameter values describing each of these buffers are presented in Supplementary Table 2. Troponin was considered to be stationary, and the corresponding diffusion coefficient was therefore set to zero. The reactive fluxes were modeled by the general ordinary differential equations:

$$J_B = k_{on}\mathrm{Ca}\,(B_{tot} - B) - k_{off}B$$

where B_{tot} is the total buffer concentration, and k_{on} and k_{off} are the on and off rate constants of the respective buffer. The free $[Ca^{2+}]_i$ was calculated using the following equation:

$$\frac{\partial \mathrm{Ca}}{\partial t} = D_{\mathrm{Ca}}\nabla^2\mathrm{Ca} - \sum_{i=1}^{4} J_{B_i} - J_{\mathrm{SERCA}} + J_{\mathrm{efflux}}$$

where D_{Ca} is the Ca^{2+} diffusion coefficient, and J_{SERCA} represents Ca^{2+} reuptake flux by the SR Ca^{2+} ATPase (SERCA). The formulation describing SERCA activity was adopted from ref. [41], and modified to subtract SR Ca^{2+} leak (J_{LEAK}):

$$J_{\mathrm{SERCA}} = \frac{g_{\mathrm{SERCA}}\left[\mathrm{Ca}^{2+}\right]_i^2}{K_{\mathrm{SERCA}}^2 + \left[\mathrm{Ca}^{2+}\right]_i^2} - J_{\mathrm{LEAK}}$$

where g_{SERCA} is the maximal SERCA conductance (0.45 μM ms^{-1}) and K_{SERCA} is the dissociation constant (0.5 μM). J_{LEAK} was calculated using the equation above and setting $J_{SERCA} = 0$ and free $[Ca^{2+}]_i = 0.1$ μM.

Partial differential equations were solved using a finite element software package FEniCS (ref. [42]) with an integration step of 10 μs. Simulations were carried out using four sets of buffering parameters; three of these were based on published results[2,43,44], and a fourth parameter set based on a mix of these values (Supplementary Table 2). An example modeled spark obtained using the mixed parameter set is shown in the right panel of Extended Data Fig. 5b.

For further analysis, simulated dye-bound Ca^{2+} concentration was summed over 2 ms intervals, equivalent to the frame time employed in spark imaging experiments, and data were convolved with a TIRF point-spread function. From these data, basic spark characteristics including spark amplitude, full width at half maximum, FDHM and time to peak (TTP) were calculated. Various focal planes were examined to investigate effects on spark characteristics (Extended Data Fig. 5c), and allow threshold setting for exclusion of out-of-focus events in experimental recordings.

Using experimentally measured Ca^{2+} spark amplitudes, we estimated the maximal number of simultaneously open RyRs that could underlie each event. To this end, simulated spark amplitudes obtained from different cluster sizes were fitted with a Michaelis–Menten-type equation:

$$A(n) = nA_{\max}/(n + \mathrm{K_A})$$

where A is spark amplitude that is dependent on cluster size n, and A_{max} and K_A are maximal amplitude and the half-saturation constant, respectively. A_{max} and K_A were determined by least-squares fitting (Extended Data Fig. 5d). Note that the equation was used to fit the data phenomenologically to reproduce the relationship between spark amplitude and cluster size. This fitting was carried out for all four buffer parameter sets, as presented in Extended Data Fig. 5e. The included uncertainty estimation (gray fill) is based on sensitivity analysis of the experimental spark fitting algorithm, set as two s.d. of the amplitudes' fitting error (at $F_0 = 40$, assuming rather high noise level). This value was added to the upper and subtracted from the lower fitted curves in Extended Data Fig. 5e.

Sensitivity analysis of spark fitting algorithm. For experimental Ca^{2+} spark detection and assessment of basic spark parameters, we employed a 2D elliptical Gaussian function:

$$I(x,y) = A\exp\left(-a(x-x_0)^2 - 2b(x-x_0)(y-y_0) - c(y-y_0)^2\right) + d$$

where I is fluorescence intensity at coordinates x,y, A is the amplitude at x_0,y_0, d is background offset and coefficients a,b,c are defined as follows:

$$a = \frac{\cos^2\theta}{2\sigma_x^2} + \frac{\sin^2\theta}{2\sigma_y^2}, b = -\frac{\sin 2\theta}{4\sigma_x^2} + \frac{\sin 2\theta}{4\sigma_y^2}, c = \frac{\sin^2\theta}{2\sigma_x^2} + \frac{\cos^2\theta}{2\sigma_y^2},$$

Here, θ is the rotation angle, and σ_x,σ_y are width parameters (standard deviation of the Gaussian function). Using least-squares fitting, the following parameters were determined: $A, x_0, y_0, \theta, \sigma_x, \sigma_y$.

The accuracy of spark fitting was determined as illustrated in Extended Data Fig. 6, for two examples. Sets of synthetic sparks were generated using the 2D elliptical Gaussian function (left panels). These sparks were then degraded by both Poisson and Gaussian noise, estimated from experiments. Poisson noise is multiplicative depending on the signal level, and therefore directly related to the F_0 value. Fitting with the 2D Gaussian function was carried out in two steps: (1) initial fitting parameter values were found using a blurred version of the degraded image; and (2) final parameter values were determined using the degraded image itself. For the examples illustrated in Extended Data Fig. 6a, the contour lines shown in the right column indicate that the algorithm accurately reproduced the shape of the spark.

To further quantify the performance of the algorithm, we generated images with varying spark amplitudes and background offsets. For each combination, 2,000 simulations were carried out to determine the deviation in each fit parameter (δ) from the ground truth. In the particular case where the noise level was rather high (low F_0 value; Extended Data Fig. 6b), the centroid localization precision and width measures were within ±1 pixel, whereas rotation angle and amplitude fell between ±10 degrees and ±0.2 $\Delta F/F_0$, respectively. With increasing F_0, the s.d. of δ for fitting parameters decreased, as illustrated in Extended Data Fig. 6c (average values indicated by squares, 1 s.d. indicated by shaded region). A similar trend was apparent with increasing spark amplitude (Extended Data Fig. 6d), except for the s.d. of δ amplitude, which increased slightly. These s.d. of δ amplitude values were used to determine the uncertainty range when investigating the relationship between spark amplitude and RyR cluster size (Fig. 4d–f in the main text and Extended Data Fig. 7c–e).

Statistical analysis

Statistical analysis was performed in the R statistical programming language https://www.R-project.org/. The Lmer and Lmertest libraries were employed for mixed model analysis of uneven nested groups[45]. This nested analysis was required to account for differing Ca^{2+} spark frequency between cells, and different numbers of cells examined from each heart. As indicated in the Source Data, P values were estimated by

Satterthwaite's method[46] for estimation of degrees of freedom. $P < 0.05$ was considered to be statistically significant. For a broader summary of statistical results please refer to Source Data.

Reporting summary

Further information on research design is available in the Nature Portfolio Reporting Summary linked to this article.

Data availability

Data supporting the analyses in this study are included in the main article and associated files. Source data are provided with this paper.

Code availability

The custom Python code for spark detection is available at https://gitlab.com/louch-group/2d-spark-detector. The Python code for mathematical modeling of sparks is available at https://gitlab.com/louch-group/sparks-simulator.

References

1. Cheng, H., Lederer, W. J. & Cannell, M. B. Calcium sparks: elementary events underlying excitation-contraction coupling in heart muscle. *Science* **262**, 740–744 (1993).
2. Kolstad, T. R. et al. Ryanodine receptor dispersion disrupts Ca^{2+} release in failing cardiac myocytes. *eLife* **7**, e39427 (2018).
3. Galice, S., Xie, Y., Yang, Y., Sato, D. & Bers, D. M. Size matters: ryanodine receptor cluster size affects arrhythmogenic sarcoplasmic reticulum calcium release. *J. Am. Heart Assoc.* **7**, e008724 (2018).
4. Walker, M. A. et al. Superresolution modeling of calcium release in the heart. *Biophys. J.* **107**, 3018–3029 (2014).
5. Franzini-Armstrong, C. & Protasi, F. Ryanodine receptors of striated muscles: a complex channel capable of multiple interactions. *Physiol. Rev.* **77**, 699–729 (1997).
6. Yin, C. C. & Lai, F. A. Intrinsic lattice formation by the ryanodine receptor calcium-release channel. *Nat. Cell Biol.* **2**, 669–671 (2000).
7. Hayashi, T. et al. Three-dimensional electron microscopy reveals new details of membrane systems for Ca^{2+} signaling in the heart. *J. Cell Sci.* **122**, 1005–1013 (2009).
8. Asghari, P. et al. Nonuniform and variable arrangements of ryanodine receptors within mammalian ventricular couplons. *Circ. Res.* **115**, 252–262 (2014).
9. Shen, X. et al. 3D dSTORM imaging reveals novel detail of ryanodine receptor localization in rat cardiac myocytes. *J. Physiol.* **597**, 399–418 (2019).
10. Jayasinghe, I. et al. True molecular scale visualization of variable clustering properties of ryanodine receptors. *Cell Rep.* **22**, 557–567 (2018).
11. Sheard, T. M. et al. Three-dimensional and chemical mapping of intracellular signaling nanodomains in health and disease with enhanced expansion microscopy. *ACS Nano* **13**, 2143–2157 (2019).
12. Hou, Y., Jayasinghe, I., Crossman, D. J., Baddeley, D. & Soeller, C. Nanoscale analysis of ryanodine receptor clusters in dyadic couplings of rat cardiac myocytes. *J. Mol. Cell. Cardiol.* **80**, 45–55 (2015).
13. Sobie, E. A., Dilly, K. W., dos Santos Cruz, J., Lederer, W. J. & Jafri, M. S. Termination of cardiac Ca^{2+} sparks: an investigative mathematical model of calcium-induced calcium release. *Biophys. J.* **83**, 59–78 (2002).
14. Asghari, P. et al. Cardiac ryanodine receptor distribution is dynamic and changed by auxiliary proteins and post-translational modification. *eLife* **9**, e51602 (2020).
15. Hiess, F. et al. Dynamic and irregular distribution of RyR2 clusters in the periphery of live ventricular myocytes. *Biophys. J.* **114**, 343–354 (2018).
16. Shen, X. et al. Prolonged β-adrenergic stimulation disperses ryanodine receptor clusters in cardiomyocytes and has implications for heart failure. *eLife* **11**, e77725 (2022).
17. Macquaide, N. et al. Ryanodine receptor cluster fragmentation and redistribution in persistent atrial fibrillation enhance calcium release. *Cardiovasc. Res.* **108**, 387–398 (2015).
18. Hiess, F. et al. Distribution and function of cardiac ryanodine receptor clusters in live ventricular myocytes. *J. Biol. Chem.* **290**, 20477–20487 (2015).
19. Baddeley, D., Jayasinghe, I. D., Cremer, C., Cannell, M. B. & Soeller, C. Light-induced dark states of organic fluochromes enable 30 nm resolution imaging in standard media. *Biophys. J.* **96**, L22–L24 (2009).
20. Tian, Q., Kaestner, L., Schröder, L., Guo, J. & Lipp, P. An adaptation of astronomical image processing enables characterization and functional 3D mapping of individual sites of excitation-contraction coupling in rat cardiac muscle. *eLife* **6**, e30425 (2017).
21. Hoteit, S., Secci, S., Sobolevsky, S., Ratti, C. & Pujolle, G. Estimating human trajectories and hotspots through mobile phone data. *Comput. Netw.* **64**, 296–307 (2014).
22. Baddeley, D. et al. Optical single-channel resolution imaging of the ryanodine receptor distribution in rat cardiac myocytes. *Proc. Natl Acad. Sci. USA* **106**, 22275–22280 (2009).
23. Laver, D. R., Kong, C. H., Imtiaz, M. S. & Cannell, M. B. Termination of calcium-induced calcium release by induction decay: an emergent property of stochastic channel gating and molecular scale architecture. *J. Mol. Cell. Cardiol.* **54**, 98–100 (2013).
24. Tian, Q. et al. Large scale, unbiased analysis of elementary calcium signaling events in cardiac myocytes. *J. Mol. Cell. Cardiol.* **135**, 79–89 (2019).
25. Hurley, M. E. et al. A correlative super-resolution protocol to visualise structural underpinnings of fast second-messenger signalling in primary cell types. *Methods* **193**, 27–37 (2020).
26. Ladd, D. et al. Assessing cardiomyocyte excitation-contraction coupling site detection from live cell imaging using a structurally-realistic computational model of calcium release. *Front. Physiol.* **10**, 1263 (2019).
27. Hake, J. et al. A stochastic model of the ryanodine receptor featuring coupled gating and competitive binding of luminal and cytosolic Ca^{2+} and Mg^{2+}. *Biophys. J.* **100**, 556a (2011).
28. Louch, W. E. et al. Slow Ca^{2+} sparks de-synchronize Ca^{2+} release in failing cardiomyocytes: evidence for altered configuration of Ca^{2+} release units? *J. Mol. Cell. Cardiol.* **58**, 41–52 (2013).
29. Meng, X. et al. Three-dimensional localization of serine 2808, a phosphorylation site in cardiac ryanodine receptor. *J. Biol. Chem.* **282**, 25929–25939 (2007).
30. Swietach, P., Spitzer, K. W. & Vaughan-Jones, R. D. Modeling calcium waves in cardiac myocytes: importance of calcium diffusion. *Front. Biosci. (Landmark ed.)* **15**, 661 (2010).
31. Cannell, M. B., Kong, C. H. T., Imtiaz, M. S. & Laver, D. R. Control of sarcoplasmic reticulum Ca^{2+} release by stochastic RyR gating within a 3D model of the cardiac dyad and importance of induction decay for CICR termination. *Biophys. J.* **104**, 2149–2159 (2013).
32. Franzini-Armstrong, C., Protasi, F. & Ramesh, V. Shape, size, and distribution of Ca^{2+} release units and couplons in skeletal and cardiac muscles. *Biophys. J.* **77**, 1528–1539 (1999).
33. Cheng, H., Lederer M.R., Lederer, W.J., & Cannell M.B. Calcium sparks and $[Ca^{2+}]_i$ waves in cardiac myocytes. *Am. J. Physiol.* **270**, C148–159 (1996).
34. Baldering, T. N. et al. Synthetic and genetic dimers as quantification ruler for single-molecule counting with PALM. *Mol. Biol. Cell* **30**, 1369–1376 (2019).

35. Lee, S.-H., Shin, J. Y., Lee, A. & Bustamante, C. Counting single photoactivatable fluorescent molecules by photoactivated localization microscopy (PALM). *Proc. Natl Acad. Sci. USA* **109**, 17436–17441 (2012).
36. Louch, W. E. et al. T-tubule disorganization and reduced synchrony of Ca^{2+} release in murine cardiomyocytes following myocardial infarction. *J. Physiol.* **574**, 519–533 (2006).
37. Finsen, A. V., Christensen, G. & Sjaastad, I. Echocardiographic parameters discriminating myocardial infarction with pulmonary congestion from myocardial infarction without congestion in the mouse. *J. Appl. Physiol. (1985)* **98**, 680–689 (2005).
38. Aronsen, J. M. et al. Noninvasive stratification of postinfarction rats based on the degree of cardiac dysfunction using magnetic resonance imaging and echocardiography. *Am. J. Physiol. Heart. Circ. Physiol.* **312**, H932–H942 (2017).
39. Hou, Y., Le, C., Soeller, C. & Louch, W. E. Protocol for the isolation and super-resolution dSTORM imaging of RyR2 in Cardiac myocytes. *Bio-protocol* **101**, e2952 (2018).
40. Ramay, H. R., Liu, O. Z. & Sobie, E. A. Recovery of cardiac calcium release is controlled by sarcoplasmic reticulum refilling and ryanodine receptor sensitivity. *Cardiovasc. Res.* **91**, 598–605 (2011).
41. Niederer, S. A. & Smith, N. P. A mathematical model of the slow force response to stretch in rat ventricular myocytes. *Biophys. J.* **92**, 4030–4044 (2007).
42. Logg, A., Mardal, K.-A. & Wells, G. *Automated Solution of Differential Equations by the Finite Element Method: The FEniCS Book* (Springer, 2012).
43. Kong, C. H. T., Laver, D. R. & Cannell, M. B. Extraction of sub-microscopic Ca fluxes from blurred and noisy fluorescent indicator images with a detailed model fitting approach. *PLoS Comput. Biol.* **9**, e1002931 (2013).
44. Rajagopal, V. et al. Examination of the effects of heterogeneous organization of RyR clusters, myofibrils and mitochondria on Ca^{2+} release patterns in cardiomyocytes. *PLoS Comput. Biol.* **11**, e1004417 (2015).
45. Bates, D., Mächler, M., Bolker, B. & Walker, S. Fitting linear mixed-effects models using lme4. *J. Stat. Soft.* **16**, 1–48 (2015)
46. Satterthwaite, F. E. An approximate distribution of estimates of variance components. *Biometrics* **2**, 110–114 (1946).
47. Nieuwenhuizen, R. P. et al. Measuring image resolution in optical nanoscopy. *Nat. Methods* **10**, 557–562 (2013).

Acknowledgements

We thank the Section for Comparative Medicine, Oslo University Hospital Ullevål (Oslo, Norway) for animal care. This work was supported by the European Union's Horizon 2020 research and innovation program (Consolidator grant agreement No. 647714 to W.E.L.) and by the Norwegian Research Council (project No. 287395 to W.E.L.).

Author contributions

Y.H., M.L, P.P.J, C.S. and W.E.L. were responsible for the conception and design of the study. Y.H., M.L., J.L., X.S. and C.L. carried out cellular imaging studies and analysis. Y.H. and M.L. developed custom code for this analysis, and conducted mathematical modeling. O.M. organized the breeding of the transgenic mouse model. E.S.N. performed sham and infarction surgery, and L.Z. and I.S. assessed in vivo cardiac structure and function. Y.H. and W.E.L wrote the paper with critical input from all authors. Funding for the study was provided by W.E.L.

Competing interests

The authors declare no competing interests.

Additional information

Extended data is available for this paper at https://doi.org/10.1038/s44161-022-00199-2.

Supplementary information The online version contains supplementary material available at https://doi.org/10.1038/s44161-022-00199-2.

Correspondence and requests for materials should be addressed to Yufeng Hou or William E. Louch.

Peer review information *Nature Cardiovascular Research* thanks Ana Gomez and the other, anonymous, reviewer(s) for their contribution to the peer review of this work.

https://doi.org/10.1038/s44161-022-00199-2

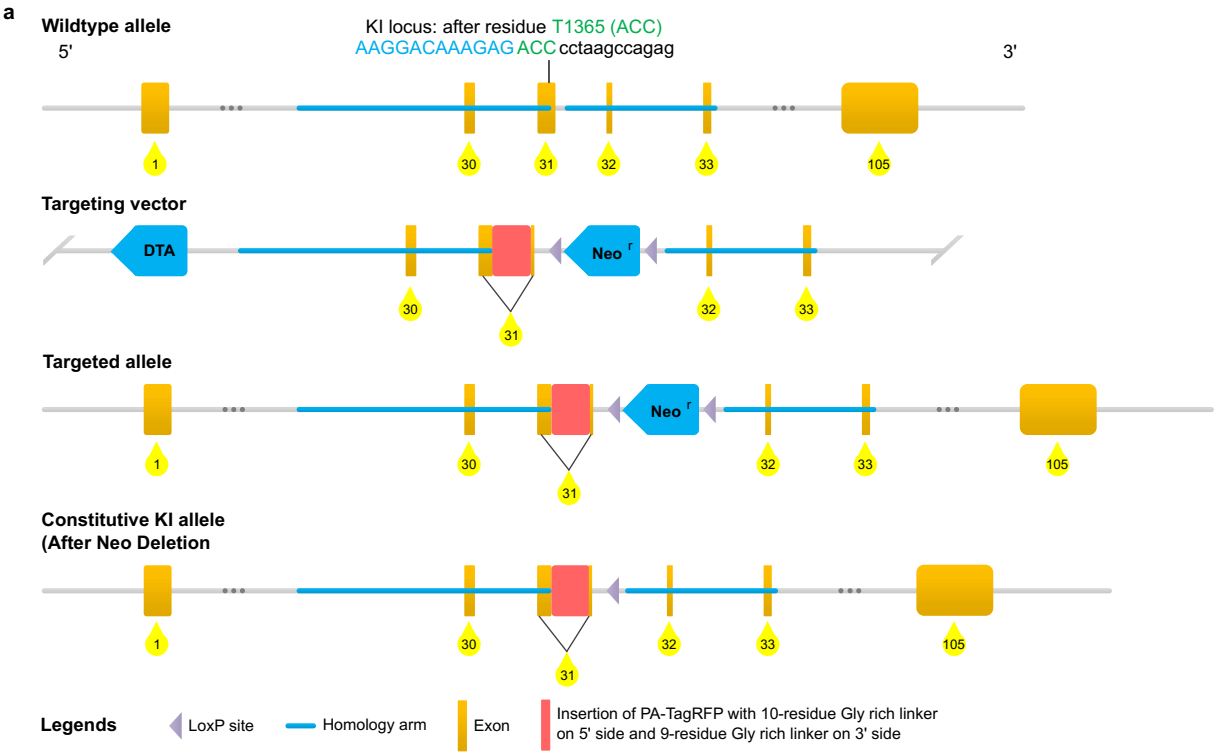

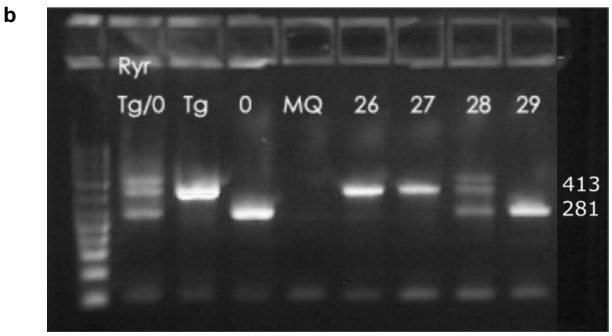

Extended Data Fig. 1 | Knock-in strategy and validation. (**a**) Schematic detailing the insertion plan using homologous recombination and neomycin cassette (provided by Cyagen, Santa Clara, CA, USA). (**b**) PCR analyses were employed to genotype mouse progeny, based on the presence of the WT (0) RyR allele (281 base pairs) or PA-Tag RFP knock-in transgene (TG, 413 base pairs). Randomly-selected mice examined in this example blot include those expressing the homozygous TG, which were used in experiments (animals #26 and 27), a heterozygous animal (#28), and an animal null for the TG (#29). TG gene expression was validated in all experimental animals.

https://doi.org/10.1038/s44161-022-00199-2

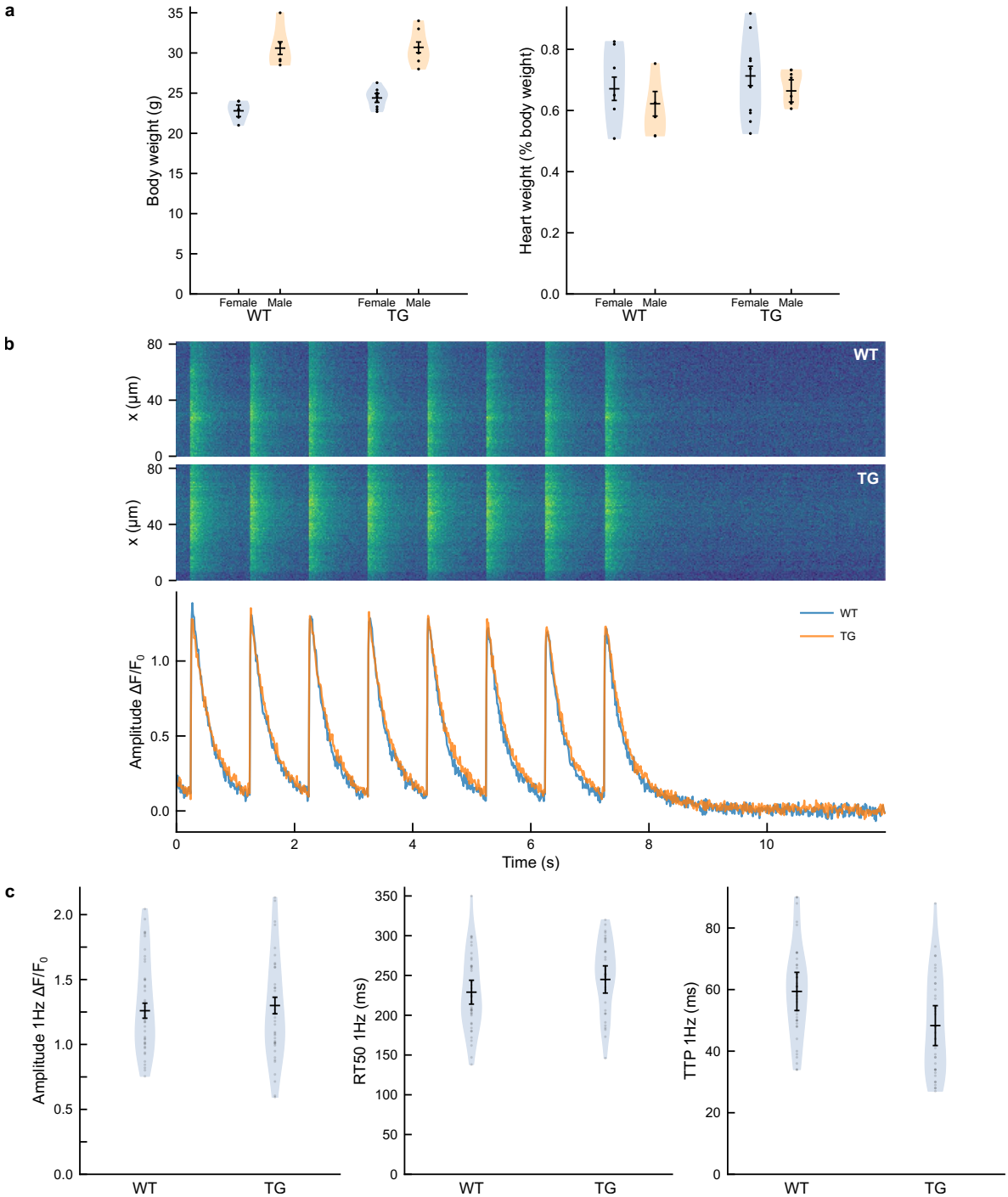

Extended Data Fig. 2 | Validation of normal animal growth and cardiomyocyte Ca^{2+} homeostasis in transgenic animals. (**a**) Animal body and heart weights were similar in knock-in (TG) and wild-type (WT) animals. n = 29 animals; 5 male WT, 6 female WT, 7 male TG, 10 female TG. (**b**) Ca^{2+} transients were measured in isolated cardiomyocytes using confocal line-scan imaging during 1 Hz field stimulation. Representative line-scans are show in the upper panels, with spatially-averaged Ca^{2+} transients below. (**c**) Mean measurements of Ca^{2+} transient parameters were similar in TG and WT cardiomyocytes. RT50 = time to half decline. TTP = time to peak. $n_{recordings}$: control = 42, TG = 39.

https://doi.org/10.1038/s44161-022-00199-2

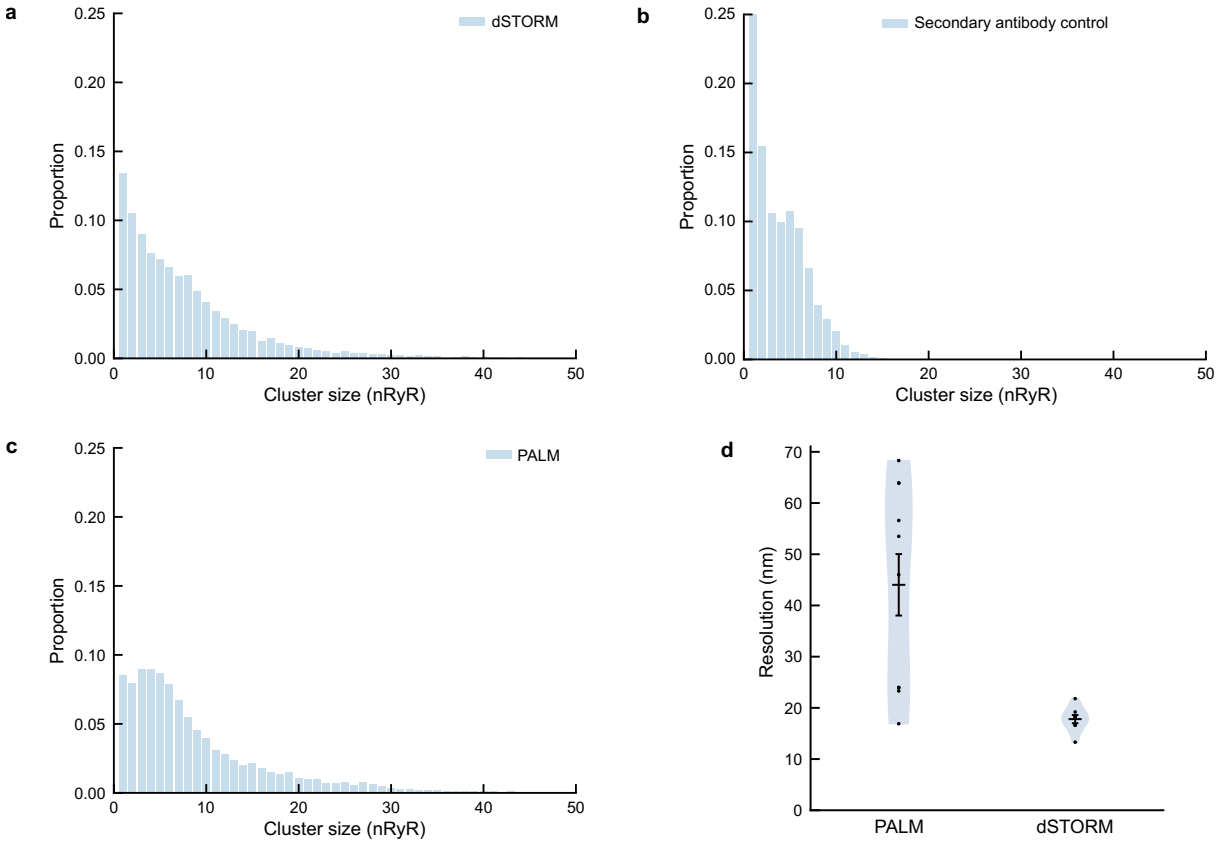

Extended Data Fig. 3 | RyR cluster size measurements and resolution obtained in dSTORM and PALM imaging experiments. (**a**) Distribution of RyR cluster size measurements from dSTORM imaging at the cell surface. (**b**) Control experiments performed with secondary antibody alone indicated nonspecific labeling, artefactually manifested as small RyR clusters. (**c**) Distribution of RyR cluster size measurements by PALM imaging at the cell surface. In comparison with dSTORM results, proportionally fewer small RyR clusters were identified by PALM imaging, as issues with non-specificity of antibody labeling were avoided. (**d**) Resolution obtained for dSTORM and PALM imaging, as estimated by Fourier ring correlation[47]. Data are mean ± standard error. n = 10 PALM images, 7 dSTORM images.

https://doi.org/10.1038/s44161-022-00199-2

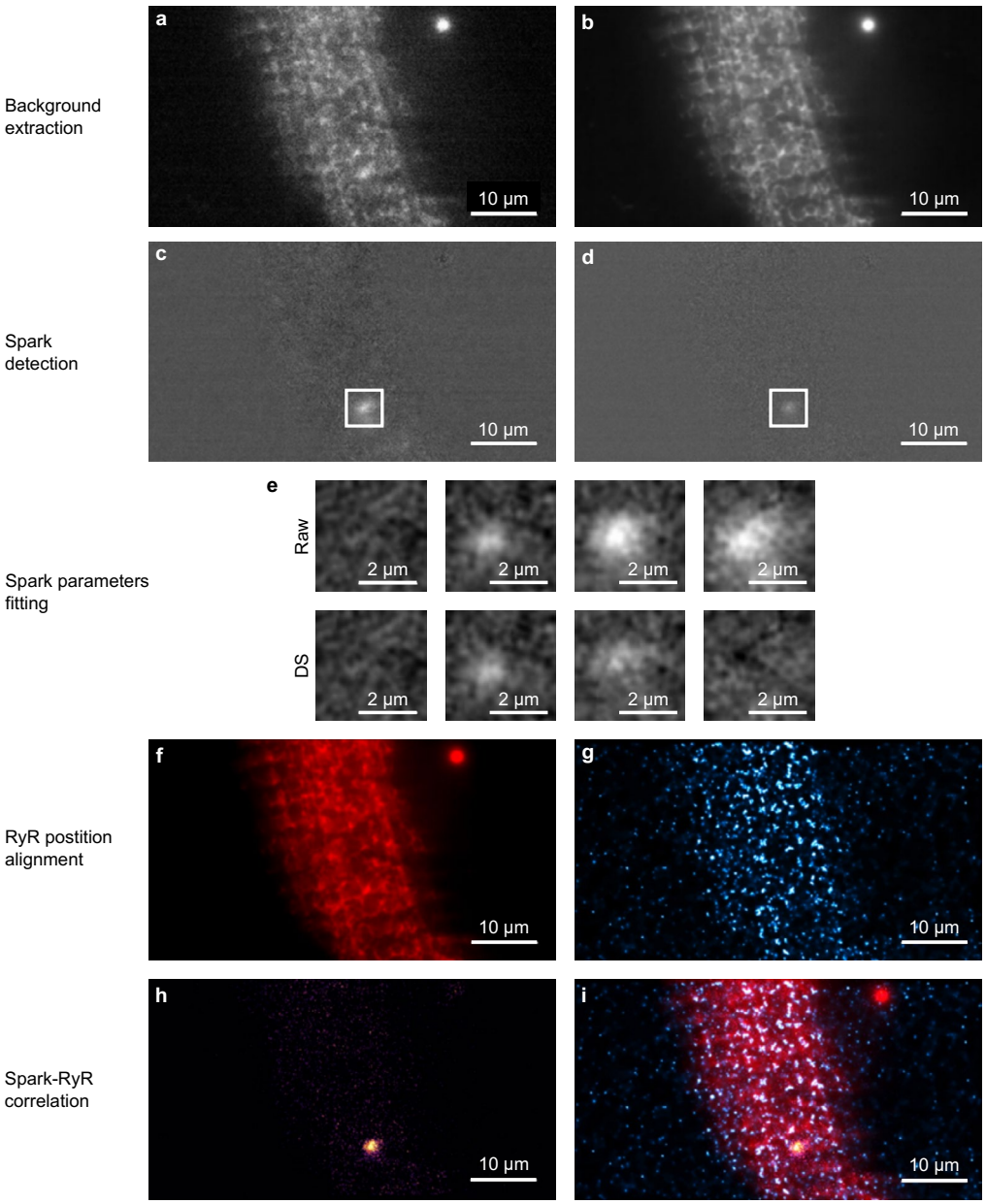

Extended Data Fig. 4 | Representative examples illustrating steps in image processing. (**a**) Raw fluorescence image. (**b**) Pixel-wise extrapolated background. (**c**) Background-subtracted image, with a putative Ca^{2+} spark indicated. (**d**) Temporally-averaged data for initial coarse identification of Ca^{2+} spark. (**e**) Extracted spark time course, with frames separated by 20 ms. Raw and diffusion-subtracted outputs are presented, blurred by a 2-pixel Gaussian filter to reduce false detections. (**f**) Averaged background revealing SR structure. (**g**) PALM RyR image used to align the signal with SR structure, accounting for chromatic shift. This alignment enabled direct correlation of confirmed Ca^{2+} sparks (**h**) to RyR positions (**i**, merged image). The described analysis steps were performed for all recordings of Ca^{2+} sparks and RyRs. ~80% of Ca^{2+} release events were successfully aligned with RyRs, i.e. situated within 300 nm of a cluster (see Fig. 3c).

https://doi.org/10.1038/s44161-022-00199-2

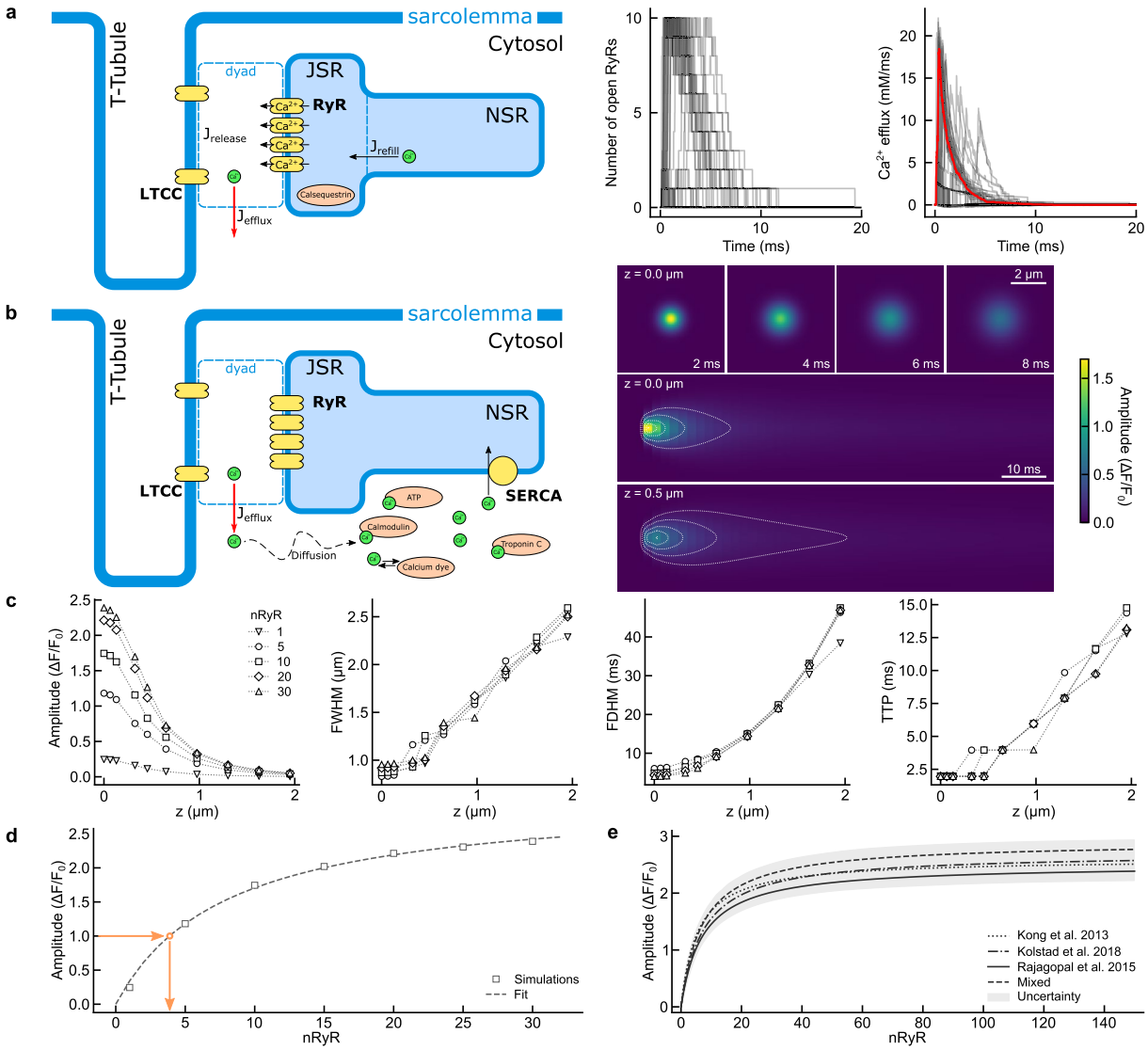

Extended Data Fig. 5 | Modeling approaches to examine RyR collaboration during Ca^{2+} sparks. (a) Left panel: schematic of a model employed for calculating average Ca^{2+} efflux from SR during a spark. 100 Ca^{2+} spark simulations are presented for a cluster of 10 RyRs, with the number of open RyRs and Ca^{2+} release rate shown in the middle and right panels (the average flux shown in red). As illustrated in **(b)**, the average Ca^{2+} efflux was used in a reaction-diffusion model. An example of a simulated Ca^{2+} spark is shown at the right. The top row shows changes in Ca^{2+} fluorescence at the focal plane (z = 0.0). The middle and bottom rows show the same spark's line-scans at different focal planes. The white contours from inside-out indicate 1, 0.75, 0.5, 0.25, and 0.1x maximum fluorescence. **(c)** Dependence of spark characteristics on the focal plane, indicating that out-of-focus events present with smaller amplitudes and broader geometries. FWHM values were used as a metric to exclude out-of-focus sparks in experimental recordings, using a cutoff value of 0.8 µm. **(d)** Simulated spark amplitudes from different cluster sizes were fitted with a Michaelis–Menten type equation to estimate the maximal number of simultaneously open RyRs for measured sparks (see orange arrows). **(e)** The simulations were repeated using different parameter values for Ca^{2+} buffers (see Supplementary Table 2). The uncertainty (gray fill) is based on sensitivity analysis of the spark detection algorithm (see Methods).

https://doi.org/10.1038/s44161-022-00199-2

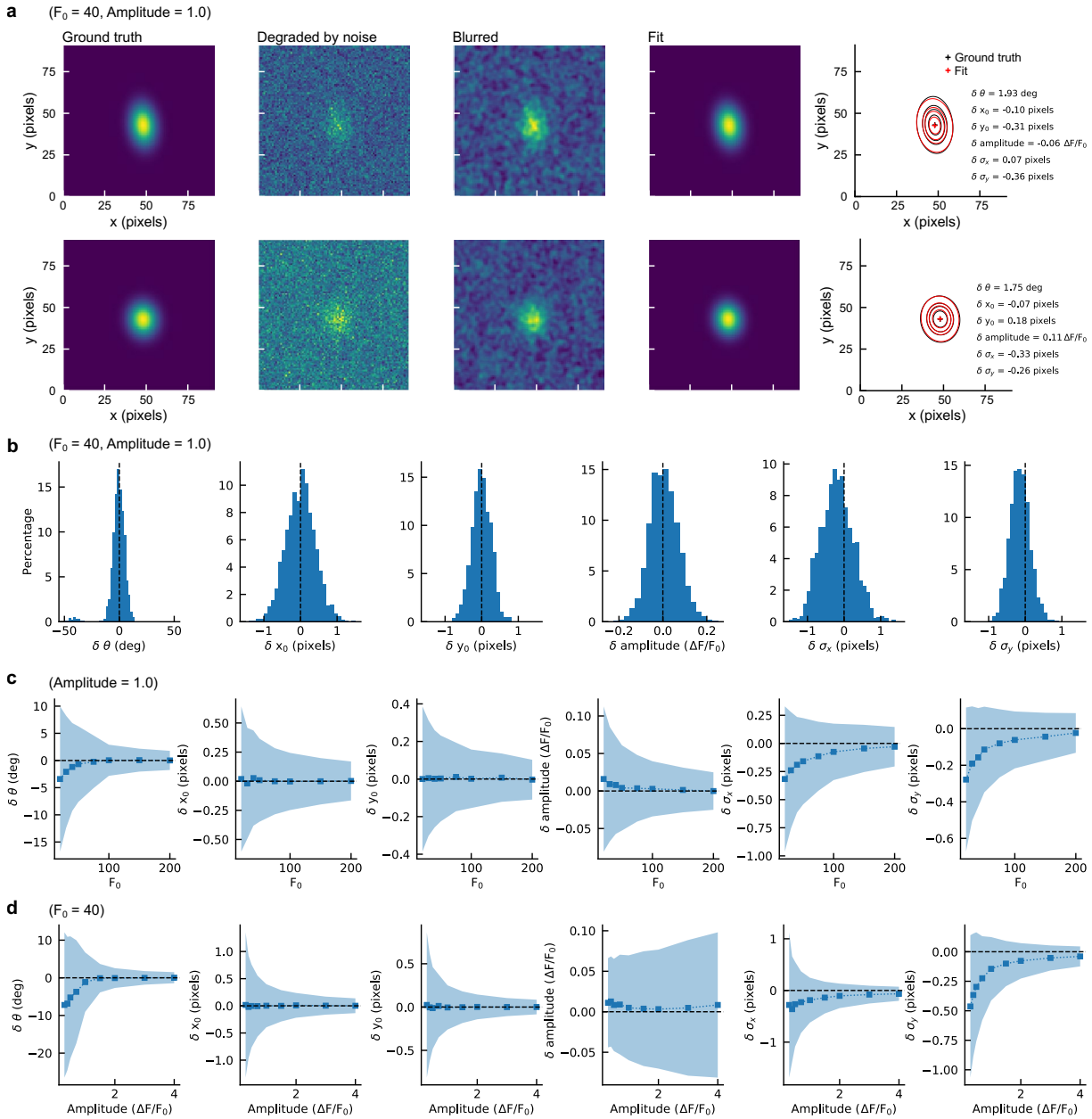

Extended Data Fig. 6 | Sensitivity analysis of the spark fitting algorithm. (**a**) Spark fitting performance is illustrated for two synthetic example sparks (left panels). Sparks were degraded by Poisson and Gaussian noise, blurred, and then fitted by a 2D elliptical Gaussian function as described in Methods. Black and red contours (from outside in) in the right panel correspond to 10%, 34.1% (one SD), 50%, and 75% of the amplitude of the ground truth and fitted result, respectively. (**b**) Fitting error (δ) indicating deviation from ground truth, based on 2000 simulations at fixed F_0 and spark amplitude (40 and 1.0, respectively). Measurements are presented for (from left to right), angle of rotation (θ), x and y positions of the centroid (x_0 and y_0), spark amplitude, and spark width in x and y dimensions (σ_x and σ_y). (**c**), (**d**) show changes in average deviance (squares) and SD (shaded) of the fitting error over a range of F_0 and amplitudes, respectively. Each data point is derived from 2000 simulations.

https://doi.org/10.1038/s44161-022-00199-2

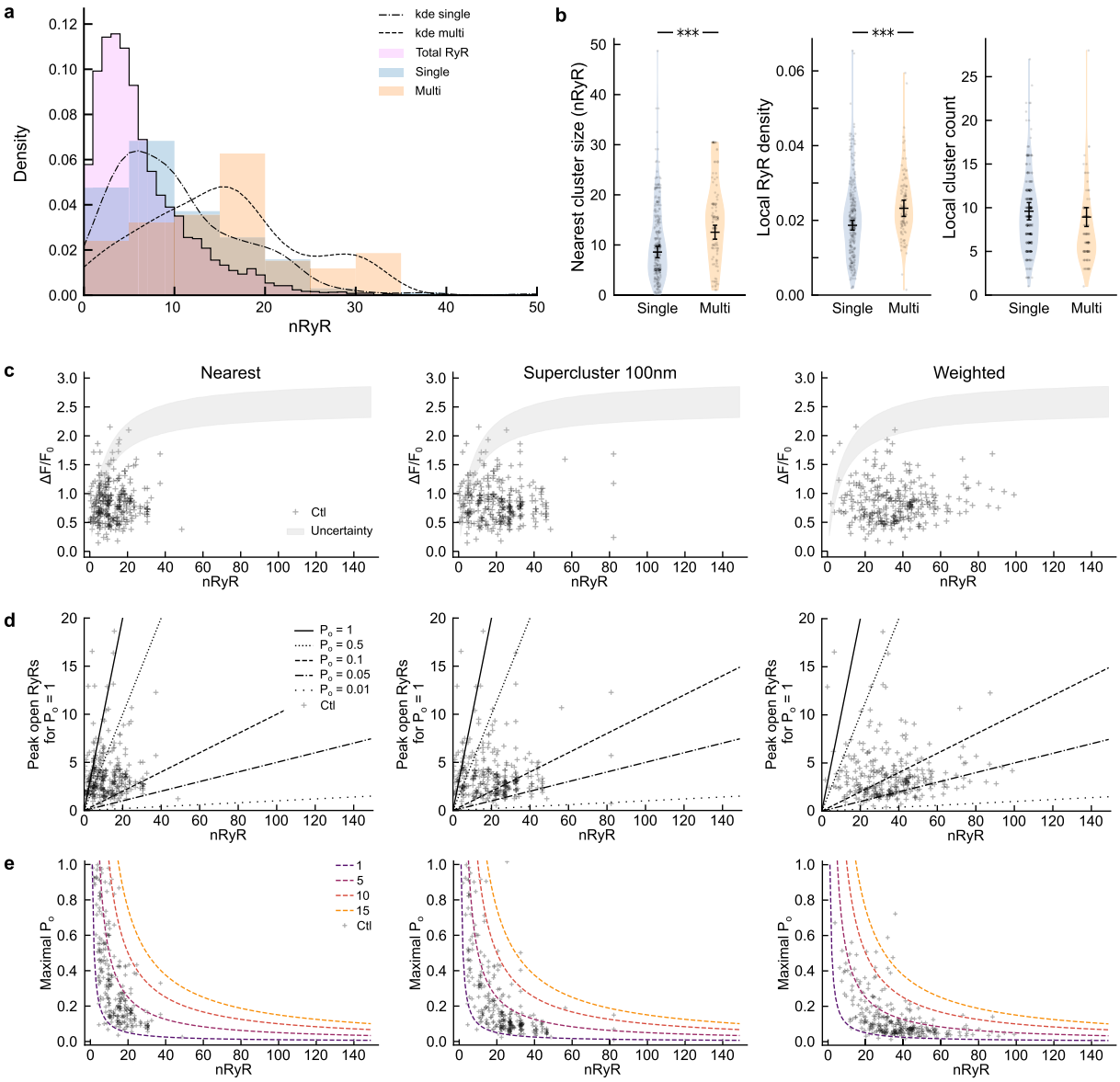

Extended Data Fig. 7 | Quantitative analysis of Ca^{2+} release sites, assuming looser RyR packing. Data are presented as in Fig. 4, but with estimates of RyR number based on packing density reported from DNA-PAINT studies[10]. We note that this is a scalar adjustment, and thus proportional differences between groups remained similar. (**a**) Nearest RyR cluster sizes for single-release (blue) and multirelease sparks (orange), compared to the overall distribution of RyR cluster sizes (pink). (**b**) Mean estimates of RyR configurations underlying Ca^{2+} sparks. Please refer to Extended Data Fig. 9 for evidence that there was no apparent density shift in RyR packing for single- and multirelease sparks. Data are presented as mean ± SEM. Differences between groups were tested with two-tailed linear mixed models with Tukey post hoc correction for multiple comparisons. *** = $P < 0.001$. P values: cluster size: 4.57×10^{-5}, local RyR density: 4.3×10^{-4}, local cluster count: 0.1748. For n values, see Supplementary Table 3, middle column. (**c**) Mathematical modeling prediction of maximal spark amplitude based on the underlying RyR cluster arrangement, with experimental data superimposed. (**d**) Estimated number of peak open RyRs for each recorded Ca^{2+} spark. (**e**) Estimated RyR open probability.

https://doi.org/10.1038/s44161-022-00199-2

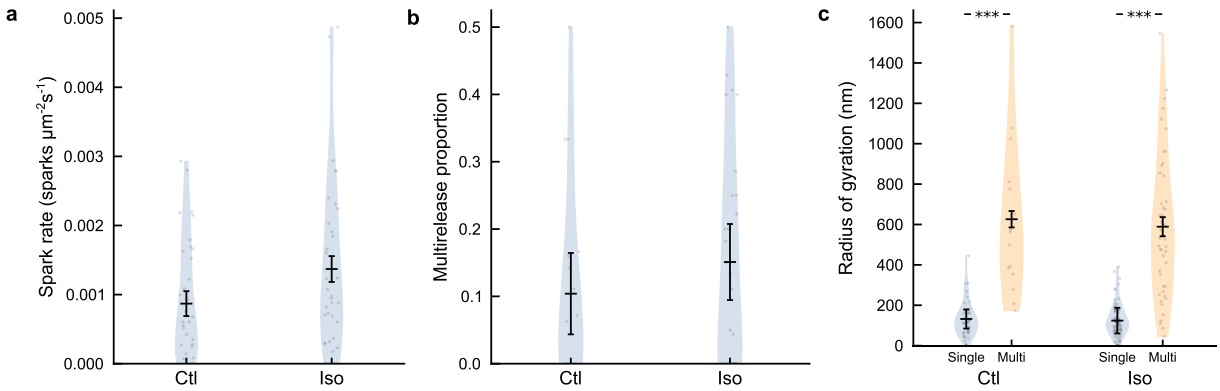

Extended Data Fig. 8 | Spark characteristics in wild-type cells. In cardiomyocytes isolated from wild-type mice, ISO treatment increased spark rate within the cell interior (**a**), but not the proportion of multirelease events (**b**) or the displacement of the spark centroid during its time course (radius of gyration, **c**). These findings closely paralleled observations made in knock-in cardiomyocytes (Fig. 7). Data are presented as mean ± SEM. Differences between groups were tested with two-tailed linear mixed models with Tukey post hoc correction for multiple comparisons. *** = $P < 0.001$. P values: **a:** 0.0538; **b:** 0.287; **c:** Ctl vs Iso 0.8425, Ctl single vs Ctl multi <0.0001, Iso single vs Iso true: <0.0001. For spark rate and multirelease proportion measurements, n = control: 3 animals, 35 cells; iso: 3 animals, 34 cells. For radius of gyration measurements, n = control$_{\text{single release}}$: 3 animals, 13 cells, 45 sparks; control$_{\text{multi release}}$: 3 animals, 9 cells, 15 sparks; iso$_{\text{single release}}$: 3 animals, 21 cells, 82 sparks; iso$_{\text{multi release}}$: 3 animals, 17 cells, 47 sparks.

https://doi.org/10.1038/s44161-022-00199-2

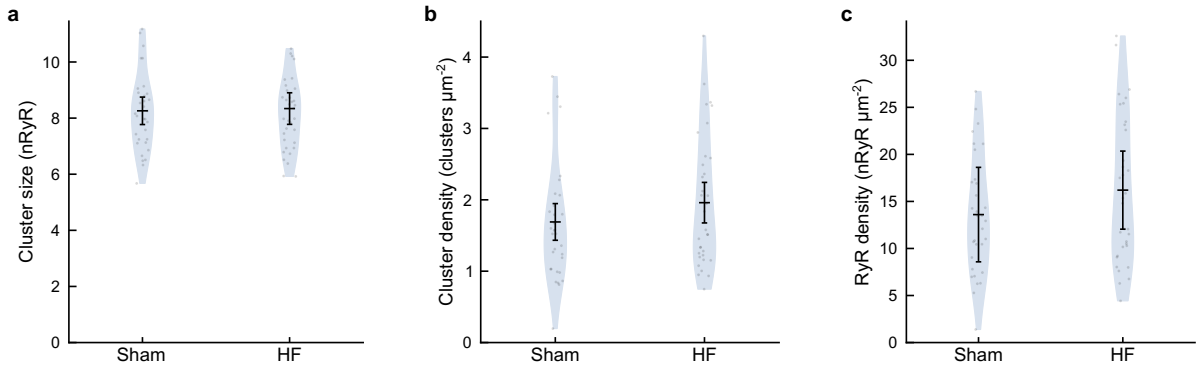

Extended Data Fig. 9 | RyR organization in sham and failing myocytes assessed by PALM imaging. RyR cluster density **(a)** and size **(b)**, as well as overall RyR density measurements **(c)** were similar in sham and postinfarction heart failure (HF) myocytes, when assessed by PALM imaging. Data are presented as mean ± SEM. Differences between groups were tested with two-tailed linear mixed models with Tukey post hoc correction for multiple comparisons. n values: sham = 32 cells, 4 animals; HF = 34 cells, 3 animals.

https://doi.org/10.1038/s44161-022-00199-2

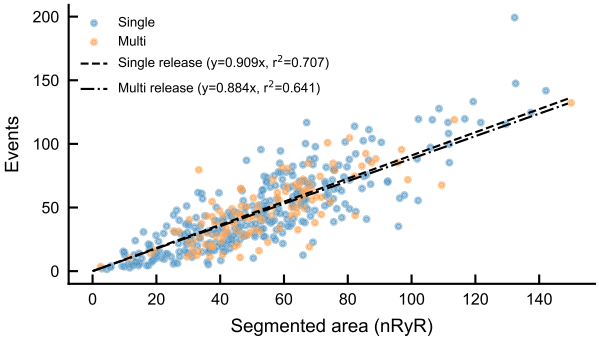

Extended Data Fig. 10 | RyR fluorescent event counts are correlated with segmented RyR area. In preliminary analysis, we tallied RyR blinking events as a possible alternative approach to quantifying RyR number. We noted an approximately linear relationship with the segmented area of the thresholded RyR signal. Importantly, very similar relationships were observed for RyR arrangements underlying single and multirelease Ca^{2+} sparks, suggesting that initiation of these distinct types of events is not dependent on differential RyR packing. Correlations were performed using least-squares fitting with a linear function. For n values, please refer to Supplementary Table 3, middle column.

nature portfolio

Corresponding author(s): William E. Louch

Last updated by author(s): 2022.11.22

Reporting Summary

Nature Portfolio wishes to improve the reproducibility of the work that we publish. This form provides structure for consistency and transparency in reporting. For further information on Nature Portfolio policies, see our Editorial Policies and the Editorial Policy Checklist.

Statistics

For all statistical analyses, confirm that the following items are present in the figure legend, table legend, main text, or Methods section.

n/a	Confirmed	
☐	☒	The exact sample size (*n*) for each experimental group/condition, given as a discrete number and unit of measurement
☐	☒	A statement on whether measurements were taken from distinct samples or whether the same sample was measured repeatedly
☐	☒	The statistical test(s) used AND whether they are one- or two-sided *Only common tests should be described solely by name; describe more complex techniques in the Methods section.*
☐	☒	A description of all covariates tested
☐	☒	A description of any assumptions or corrections, such as tests of normality and adjustment for multiple comparisons
☐	☒	A full description of the statistical parameters including central tendency (e.g. means) or other basic estimates (e.g. regression coefficient) AND variation (e.g. standard deviation) or associated estimates of uncertainty (e.g. confidence intervals)
☐	☒	For null hypothesis testing, the test statistic (e.g. *F*, *t*, *r*) with confidence intervals, effect sizes, degrees of freedom and *P* value noted *Give P values as exact values whenever suitable.*
☒	☐	For Bayesian analysis, information on the choice of priors and Markov chain Monte Carlo settings
☐	☒	For hierarchical and complex designs, identification of the appropriate level for tests and full reporting of outcomes
☐	☒	Estimates of effect sizes (e.g. Cohen's *d*, Pearson's *r*), indicating how they were calculated

Our web collection on statistics for biologists contains articles on many of the points above.

Software and code

Policy information about availability of computer code

Data collection	HCImage Live version 4.4.2.7 was used to record raw data for PALM, dSTORM, and Ca spark measurements.
Data analysis	Acquired PALM and dSTORM image data were processed and rendered using the Python Microscopy Environment version 20.12.8. Spark detection and characterization were carried out using Python scripts available at https://gitlab.com/louch-group/2d-spark-detector. Mathematical modeling of sparks was done using Python code available at https://gitlab.com/louch-group/sparks-simulator. The code was developed and tested using Python 3.6.9 and the following packages: fenics-ufl 2019.2.0.dev0, mshr 2019.2.0.dev0, h5py 2.7.1, numpy 1.16.4, scipy 1.3.0, matplotlib 3.1.0, and argparse 1.1.

For manuscripts utilizing custom algorithms or software that are central to the research but not yet described in published literature, software must be made available to editors and reviewers. We strongly encourage code deposition in a community repository (e.g. GitHub). See the Nature Portfolio guidelines for submitting code & software for further information.

Data

Policy information about availability of data

All manuscripts must include a data availability statement. This statement should provide the following information, where applicable:

- Accession codes, unique identifiers, or web links for publicly available datasets
- A description of any restrictions on data availability
- For clinical datasets or third party data, please ensure that the statement adheres to our policy

Sample sizes are presented in Supplemental Tables 3-6. Source data are provided for the performed statistical analyses.

Human research participants

Policy information about studies involving human research participants and Sex and Gender in Research.

Reporting on sex and gender	N/A
Population characteristics	N/A
Recruitment	N/A
Ethics oversight	N/A

Note that full information on the approval of the study protocol must also be provided in the manuscript.

Field-specific reporting

Please select the one below that is the best fit for your research. If you are not sure, read the appropriate sections before making your selection.

☒ Life sciences ☐ Behavioural & social sciences ☐ Ecological, evolutionary & environmental sciences

For a reference copy of the document with all sections, see nature.com/documents/nr-reporting-summary-flat.pdf

Life sciences study design

All studies must disclose on these points even when the disclosure is negative.

Sample size	Power analysis was performed to determine sample size based on known variability of measured parameters.
Data exclusions	No data were excluded from the analyses.
Replication	Consistent observations were made during analyses performed on different cardiomyocytes from different hearts. The use of nested statistics confirmed this consistency. Depending on the experiment, replication was performed on cardiomyocytes sourced from between 3 and 6 hearts, as indicated in the Supplementary Tables.
Randomization	Cardiomyocytes from mice expressing pa-RFP on the RyR were randomly selected for analysis of calcium handling, RyR localization, and treatment with isoproteronol. For surgical interventions, the pa-RFP mice were randomly selected to receive infarction or sham surgery.
Blinding	In most experiments, analysis was performed on a single type of cardiomyocyte (ie. those from healthy mice expressing pa-RFP on the RyR), and thus blinding was not necessary. For experiments on sham- and infarction-operated animals, blinding was not possible as the nature of the operation was visually apparent to laboratory staff during isolation of cells from the heart.

Reporting for specific materials, systems and methods

We require information from authors about some types of materials, experimental systems and methods used in many studies. Here, indicate whether each material, system or method listed is relevant to your study. If you are not sure if a list item applies to your research, read the appropriate section before selecting a response.

Materials & experimental systems

n/a	Involved in the study
☐	☒ Antibodies
☒	☐ Eukaryotic cell lines
☒	☐ Palaeontology and archaeology
☐	☒ Animals and other organisms
☒	☐ Clinical data
☒	☐ Dual use research of concern

Methods

n/a	Involved in the study
☒	☐ ChIP-seq
☒	☐ Flow cytometry
☒	☐ MRI-based neuroimaging

Antibodies

Antibodies used: For dSTORM analysis, a primary anti-RyR antibody was employed (MA-916, C3-33, ThermoFisher Scientific, Waltham, MA, USA). The secondary antibody employed was F(ab')2-Goat anti-Mouse IgG with Alexa Fluor 647 (A21237, ThermoFisher Scientific).

Validation: According to the manufacturer, the primary antibody was verified by relative expression to ensure that the antibody binds to the antigen stated (https://www.thermofisher.com/antibody/product/Ryanodine-Receptor-Antibody-clone-C3-33-Monoclonal/MA3-916). No non-specific staining was observed with the secondary antibody alone.

Animals and other research organisms

Policy information about studies involving animals; ARRIVE guidelines recommended for reporting animal research, and Sex and Gender in Research

Laboratory animals: This study was performed using a created transgenic mouse line on C57BL6/6N background, as described in the methods. In some experiments, comparison was made with wild-type C57BL6/6N mice. Animals were housed in a temperature- and humidity-regulated room with a 12 h day/12 h night cycle. 8-10 week-old mice of both sexes were used in experiments, apart from those used 5 weeks following surgery, which were 13-15 weeks of age when sacrificed.

Wild animals: No wild animals were used in our study.

Reporting on sex: Experiments were performed on mice of both sexes to reduce overall animal use. With this goal in mind, the study was not statistically powered to allow division of data based on sex.

Field-collected samples: No field-collected samples were used in our study.

Ethics oversight: The project was approved by the Norwegian Food Safety Authority (permit no. 8951).

Note that full information on the approval of the study protocol must also be provided in the manuscript.